DETERMINATION OF PERMEABILITY FROM PORE NETWORK MODELS BY USING A NOVEL TRANSIENT SIMULATION METHODOLOGY

A Thesis

by

SOUMYADIPTA SENGUPTA

Submitted to the Office of Graduate and Professional Studies of
Texas A&M University
in partial fulfillment of the requirements for the degree of

MASTER OF SCIENCE

Chair of Committee,	Michael J. King
Co-Chair of Committee,	Akhil Datta-Gupta
Committee Member,	Michael Pope
Head of Department,	Dan Hill

May 2016

Major Subject: Petroleum Engineering

ABSTRACT

Carbonate reservoirs are a major source of oil and gas produced across the world. Carbonate reservoirs are distinct from sandstone reservoirs in terms of deposition and characteristics. Sandstones are formed by deposition of sediments which were transported by weathering agents. The deposition of these sediments along with organic matter for millions of years formed hydrocarbons in sandstones. The porosity and permeability of the sandstones are mostly a function of the overburden of the sediment layers. Carbonate rocks are formed by deposition of carbonate particles from seawater. The organic matter in the sea is also deposited along with the carbonates. The porosity of carbonate rocks is affected by the overburden of the sediments and diagenetic processes taking place after deposition. This lends a unique character to carbonate rocks with a very heterogeneous porosity and permeability at the micro-scale and macro-scale.

This unique structure of carbonate rocks may not be amenable to simple scale models or conventional steady state permeability assessment methods. Therefore, a transient simulation based methodology was developed and implemented on a pore network extracted from a carbonate micro-CT scan image to compute permeability and additional transport properties.

This methodology was validated on a synthetic sandstone pore network model. The transient method based on the Well Test Derivative (WTD) analysis showed good agreement with the conventional method .The transient method based on Depth of Investigation (DOI) showed good agreement with the results from the conventional method for the synthetic sandstone pore network with varying degrees of heterogeneity.

The transient method based on the Well Test Derivative analysis showed good agreement with the conventional method for the carbonate pore network. However, the transient method based on DOI for the carbonate pore network, which was a dual porosity framework, infers permeability values which are quite high when compared with the steady state permeability or Well Test Derivative (WTD) permeability values. The carbonate pore network contains many high permeability and low Diffusive Time of Flight (DTOF) paths. These paths have a low combined cross-sectional area when compared to the total cross-sectional area of the whole carbonate pore network. The DOI analysis method captures the permeability of these paths which results in these high permeability values.

DEDICATION

To my family and especially my mother for her endless support and dedication

ACKNOWLEDGEMENTS

I would like to thank my committee chair, Dr. Mike King, for his insightful thoughts and guidance. I would also like to thank other committee members, Dr. Akhil Datta-Gupta, and Dr. Mike Pope for their guidance and support throughout the course of this research.

My sincere thanks to the MCERI consortium for funding my research throughout the period of my Master's study. I also want to thank all the people whom I met as a part of the MCERI group for their help and knowledge sharing.

Finally, thanks to my family for their support throughout my journey.

NOMENCLATURE

Symbols

m_{rf}	Radial Flow Well Test Derivative (Pa)
$\Delta p_{steadystate}$	Pressure difference between opposite planes in pore network (Pa)
L_{bond}	Length of Bond (m)
PV_j	Pore volume of jth node (m^3)
R_{bond}	Radius of Bond (m)
R_{grain}	Radius of sand grain (m)
T_{bond}	Inter Node Transmissibility (m^3/s/Pa)
$V_p(\tau)$	Drainage Volume as a function of Diffusive Time of Flight (m^3)
c_t	Compressibility (Pa^{-1})
k_{bond}	Permeability of Bond (m^2)
k_f	Fracture Permeability (m^2)
k_{fb}	Bulk Fracture Permeability (m^2)
k_m	Matrix Permeability (m^2)
p_{fd}	Dimensionless Fracture Pressure
p_i	Initial Pressure (Pa)
p_{md}	Dimensionless Matrix Pressure
p_{wf}	Wellbore flowing pressure (Pa)
q_{line}	Line source/sink flow rate (m^3/s)
$q_{poiseuille}$	Flow rate in bond (m^3/s)

$q_{source/sink}$	Well flow rate (m^3/s)
$q_{steadystate}$	Average steady state flow rate for pore network (m^3/s)
r_{inv}	Depth of Investigation (m)
$r_{inv,linear}$	Linear Depth of Investigation (m)
$r_{inv,radial}$	Radial Depth of Investigation (m)
r_w	Seed Node Line source radius (m)
t_d	Dimensionless Time
τ_{bond}	Diffusive Time of Flight for a bond ($\sqrt{s}$)
Δp_{bond}	Pressure difference between two ends of a bond (Pa)
B	Formation Volume Factor (Reservoir volume/Stock tank volume)
h	height of line source (m)
t	time (s)
Vf(t)	Drainage volume for nodes on plane opposite source plane (m^3)
$V(t)$	Drainage Volume as a function of time (m^3)
k	Permeability (m^2)
q	Flow rate (m^3/s)
$t\frac{\partial \Delta p}{\partial t}$	Well Test Derivative (Pa)
λ	Interporosity Flow Co-efficient
μ	Viscosity (Pa.s)
$\tau(\vec{x})$	Diffusive Time of Flight ($\sqrt{s}$)
ω	Storativity Ratio

ϕ	Porosity

Abbreviations

DOI	Depth of Investigation
DTOF	Diffusive Time of Flight
IARF	Infinite Acting Radial Flow
PSS	Pseudo Steady State
WTD	Well Test Derivative

TABLE OF CONTENTS

Page

LIST OF FIGURES

Page

LIST OF TABLES

Page

1. INTRODUCTION

Carbonate reservoirs are an important source of oil and gas throughout the world with the biggest reserves of oil reserves in the world in the Middle-East are primarily in carbonate reservoirs. Carbonate reservoirs usually have good reservoir quality and are prolific producers.

Carbonates rocks commonly have a highly heterogeneous pore structure compared to sandstone rocks. Sandstones store most fluids in the inter-granular spaces whereas carbonates have multiple modes of porosity (Choquette and Pray, 1970). The mode of transport of fluids in the carbonates is through the inter-granular pore space. There are different kinds of intra-granular porosities in carbonates and all of them interact in a different manner with inter-granular porosity. So, we can easily see that it is much easier to characterize and model flow in sandstone rocks compared to carbonate rocks due to the relatively homogeneous pore structure in sandstones as compared with carbonates.

The general definitions of relatively homogeneous or smoothly varying porosity and permeability are applicable to sandstone but not to carbonate. At any particular place in a carbonate sample, there are different kinds of porous space interacting with each other. These type of heterogeneities can't be captured by simple lab tests run on core samples. Therefore, we have tested computational methods based on a transient methodology on a carbonate pore network obtained from a carbonate core µ-CT scan sample. These methods were validated on a synthetic sandstone model. One of the methods worked well for both the synthetic sandstone pore network and carbonate pore

network whereas the other worked well for the synthetic sandstone pore network and needs more refinement for the carbonate pore network. The focus of this thesis will be to describe the computational methods used, analysis methods and the values of permeability obtained.

1.1 Literature Review

We will review the basics of carbonate deposition and the different kinds of porosity that occur in carbonate rocks. We will review some of the differences between carbonate and sandstone porosity to try and understand why carbonate characterization would be difficult using conventional means amenable to sandstone. Thereafter, we will review some of the techniques used previously to extract or make synthetic pore network models.

1.1.1 Carbonate Geology and Characterization

Sandstones and carbonate rocks are formed by differing depositional processes. Sandstone rocks are formed by the weathering down and transport by agents such as water, wind etc. to places far from their origin. The transportation also causes further physical and chemical weathering and breaking down into small pieces. These fragments are deposited in a depositional basin. Organic matter carried with the fragments is deposited in the basin. This process of deposition may occur for millions of years and lead to layers of deposition. The small fragments/grains join together to form rocks which are classified as sandstone if the grains are of an appropriate size. These rocks have inter-granular spaces which house the fluids that were formed from the organic matter deposited along with the rock fragments, or which later migrate into those spaces.

Carbonates are formed by the precipitation of calcium carbonate from seawater as carbonate shells which are deposited on the seafloor. The organisms living in the sea are deposited after their death on the seafloor and are later transformed into oil/gas after millions of years of deposition. This oil/gas may migrate to the pore spaces in the carbonate rocks to form oil and gas reservoirs.

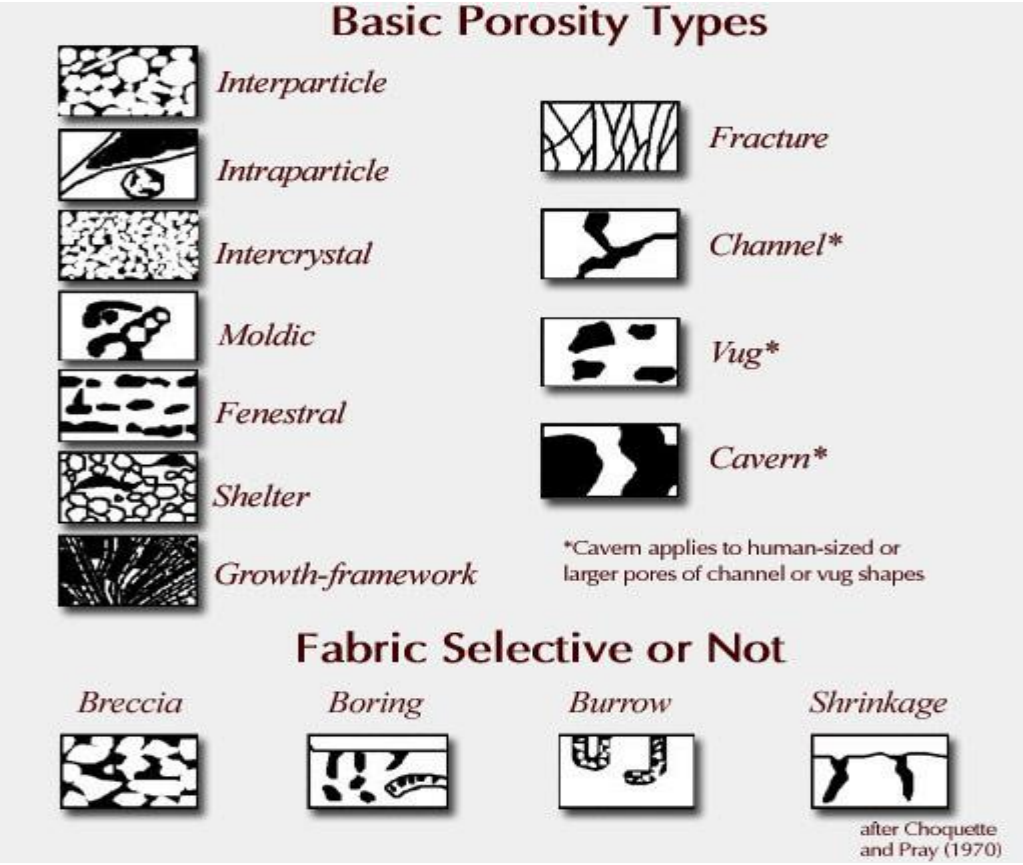

Figure 1: Porosity Types in Carbonate Rocks (after Choquette and Pray, 1970)

Pore Type	Description	Pore type	Description	Pore type	Description
Fabric selective		**Not Fabric selective**		**Fabric Selective or Not**	
Interparticle	Porosity between particles	Fracture	Porosity formed by fracturing	Breccia	Interparticle porosity in breccia
Intraparticle	Porosity within individual particles or grains	Channel	Markedly elongated pores	Boring	Porosity created by boring organism
Intercrystal	Porosity between crystals	Vug	Pores larger than 1/16 mm in diameter and somewhat equant in shape	Burrow	Porosity created by organism burrowing
Moldic	Porosity formed by selective removal of an individual constituent of the rock	Cavern	Very large channel or vug	Shrinkage	Porosity produced by sediment shrinkage
Fenestral	Pores larger than grain-supported interstices (interparticle)	Not Applicable	Not Applicable	Not Applicable	Not Applicable
Shelter	Porosity created by the sheltering effect of large sedimentary particles	Not Applicable	Not Applicable	Not Applicable	Not Applicable
Growth framework	Porosity created by in-place growth of a carbonate rock framework	Not Applicable	Not Applicable	Not Applicable	Not Applicable

Table 1: Different Porosity Types in Carbonate Rocks (after Choquette and Pray, 1970 and AAPG Wiki)

One key difference between sandstone and carbonate rocks is in the processes of diagenesis. In the case of sandstones, diagenesis might lead to some mineralogical changes like quartz cement formation, kaolinite precipitation which decreases porosity

(Surdam et al. 1989). The process of diagenesis in carbonates is far more complex, leading to generation of intra-granular porosity which leads to an increase in porosity. Carbonate diagenetic processes are the following:

1) Calcium-carbonate cementation
2) Mechanical and chemical compaction
3) Selective dissolution
4) Dolomitization
5) Evaporite mineralization
6) Massive dissolution, cavern collapse, and fracturing

The cementation and compaction processes lead to a decrease in porosity post diagenesis. The selective dissolution occurs if there are unstable minerals like high-magnesium and aragonite present in the carbonates. Dolomitization is the formation of $CaMg(CO_3)_2$ from $CaCO_3$. This process may result in an increase or decrease of porosity (Weyl, 1960). The evaporate mineralization process involves the formation of anhydrite from gypsum and this leads to a decrease in reservoir quality and porosity. Massive dissolution may occur if the carbonate comes in contact with highly acidic water which may dissolve huge volumes of the carbonate rock. Fracturing can occur as a result of the load of sediments or due to tectonic movements.

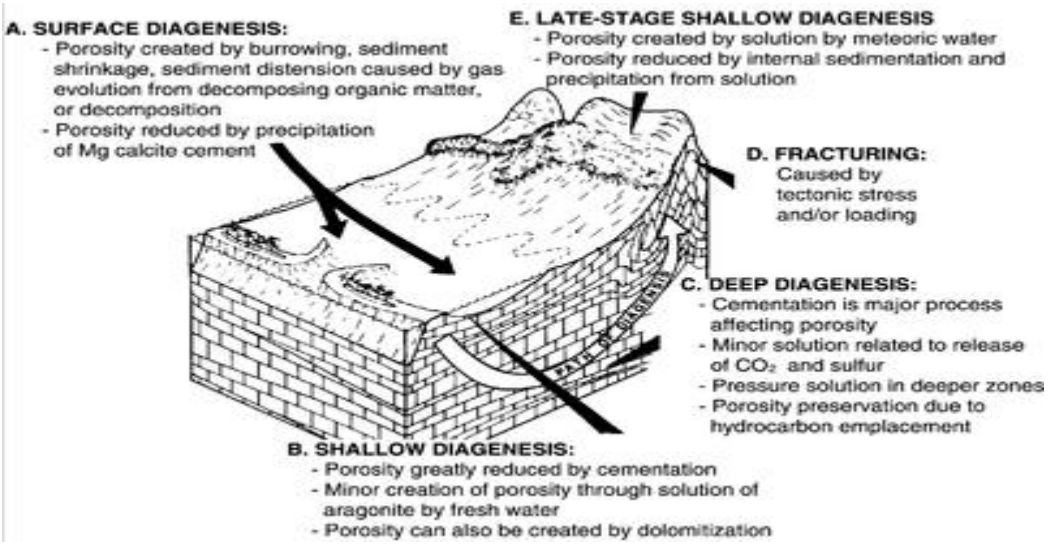

Figure 2: Diagenesis in Carbonates (Harris et al. 1985)

In this brief overview, we can see that the types of porosity available in carbonates are highly heterogeneous as compared to sandstones. Sandstone rocks have a primarily single type of porosity and permeability which is intergranular in nature. The carbonate rocks have a wide variety of porosity types that are correlated over multiple length scales. Using a grid based representation to model carbonates by averaging the heterogeneities present at different scales may lead to overly simplistic flow simulation results. The heterogeneities present in the carbonate rocks at different scales interact with each other and hence these need to be captured to accurately model flow. Therefore, a pore network based representation was used to computationally calculate the parameters like permeability in carbonate rocks so that the effect of different kinds of porosity can be captured.

1.1.2 Pore Scale Modeling

Pore scale modeling is now a widely studied topic and is being increasingly used to develop a better understanding of flow in porous media (Fatt, 1956). X-ray synchrotrons have been used to image the rock samples (Coles et al, 1998). A monochromatic beam of X-ray would be shone on the sample and different 2-D images at various angles of the X-ray absorption would be obtained. These would be combined to form a 3-D map of the X-ray absorption from which pore and grain space could be ascertained. The next development was to use CT-scanner for imaging rocks (Wellington and Vinegar, 1987). Presently, a Micro-CT scanner is used to do the same work (Arns et al. 2007). The lesser intensity of X-rays in these micro-CT scanners may provide a poorer image quality but it can be overcome by taking a very large number of images. The image resolution also depends upon the wavelength of the X-rays which are much shorter in the synchrotrons as compared to the micro-CT scans but more localized.

Several high resolution 2-D images are used to create a 3-D pore image of the concerned porous rock (Okabe and Blunt, 2004) by using multipoint statistics. This technique can recreate the connectivity of the original sample and allows pores to be represented at the various scales which is usually the case in case of carbonates.

Once the pore image is constructed, simulations are run to determine its transport characteristics and parameters. The most commonly used method is the Lattice Boltzmann type simulation method in which Lattice Boltzmann equation is solved for the entire pore space (Manwart et al. 2002). This method is computationally expensive and slow but gives accurate results. This technique is currently being used to simulate

multiphase flows in the porous media and relative permeability is estimated from such simulations (Boek et al. 2010).

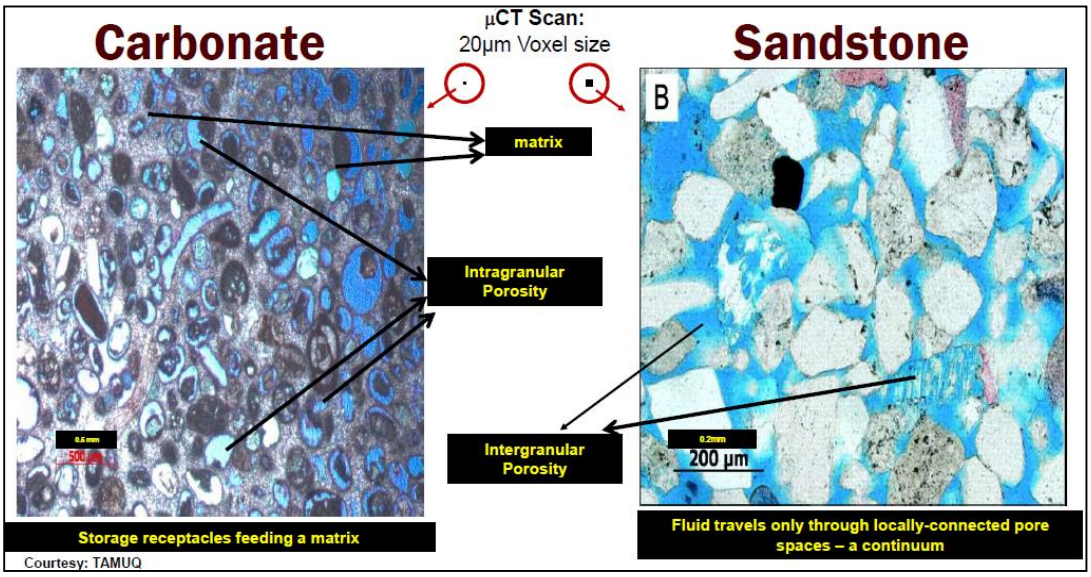

Figure 3: Pore Scale Image of a Carbonate and a Sandstone from a Micro-CT Scanner (Pasumarti, 2014)

Another method of simulating these pore spaces is by extracting network models from these pore space images. The pores are considered as void spaces containing the fluids and these pores are connected by bonds which have a certain length and radius and allow the fluid to flow from one node to another. There are various algorithms available for extracting this node and bond network from pore space 3-D images. One of them is the medial axis algorithm in which a center axis is traced through the entire pore space in 3-D (Lindquist et al. 1996). The distance from the center axis to the grain surface is used to describe a node or a bond. Another method used is the maximal ball algorithm, where

spheres are grown in the pore pace and the largest spheres represent the pore space (nodes) while a sequence of small spheres represent the bonds (Silin and Patzek, 2006). The network models extracted can be simulated to give estimates of absolute permeability, relative permeability, capillary properties etc. (Blunt et al. 2002).

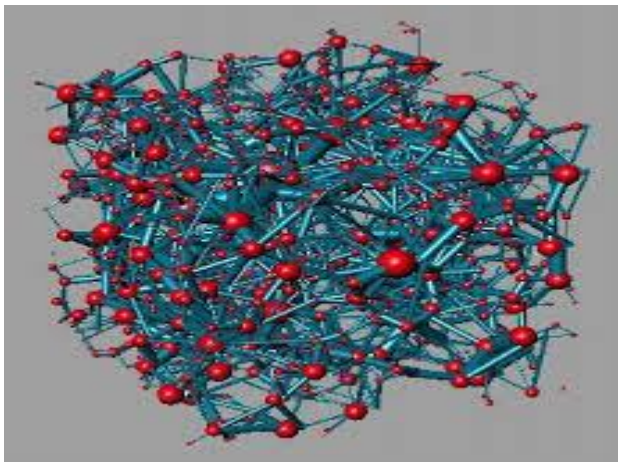

Figure 4: Pore Network (Red Balls are the Nodes and the Blue Sticks are the Bonds Connecting the Nodes) (Dong, 2008)

Figure 4 shows an image of a pore network. The red spheres are the nodes which represent the fluid containing volumes in the pore network and the blue sticks are the bonds which provide pathways for the fluid to flow between nodes.

1.1.3 Steady State Permeability Calculation

Much work has been done on steady state permeability calculation on this particular sample (Pasumarti, 2014). This sample was obtained from a Qatar carbonate reservoir and a micro-CT scan was performed on this sample. A pore network was

extracted from the micro-CT scan image the details of which are provided later in the thesis.

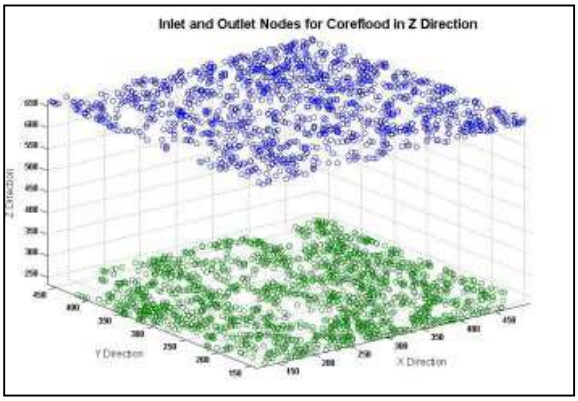

Figure 5: Planar Boundary Condition Representation for a Micro Scale Incompressible Flow Simulation (Pasumarti, 2014)

The Figure 5 shows that a small pressure gradient is applied in a particular direction in the extracted pore network to determine a net flux across the pore network. If we want to calculate the permeability in the Z-direction, then the pressure gradient is applied in the Z-direction i.e. the top and bottom plane in the Z-direction is assigned a fixed pressure due to which a small pressure gradient is developed across the sample in the Z-direction. The Equation (1.1) describes transmissibility (T_{bond}) and permeability (k_{bond}) for a particular bond.

$$T_{bond} = \frac{\pi {R_{bond}}^4}{8\mu L_{bond}}, \quad k_{bond} = \frac{R^2}{8} \tag{1.1}$$

$$\sum_{i=1}^{N}\sum_{j=1}^{M} T_{ij} * (p_i - p_j) = 0 \tag{1.2}$$

The Equation (1.2) describes the set of equations which have to be solved simultaneously for getting pressure values for all the nodes. T_{ij} is the transmissibility for the bond between the node-j and node-j and p_i, p_j are the pressures at node-i and node-j respectively. N represents the total number of nodes and M represents the number of nodes connected to a particular node. These equations are in effect mass balance equations for all the nodes. The Equation (1.3) defines the Poiseuille flow in the bonds of the pore network.

$$q_{poiseuille} = \frac{\pi R_{bond}^4 \Delta p_{bond}}{8\mu L_{bond}} \tag{1.3}$$

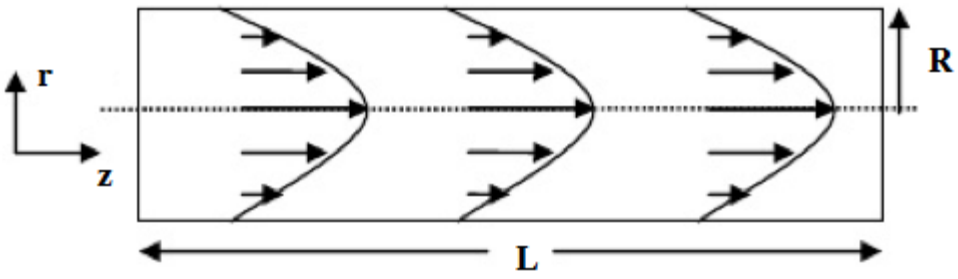

Figure 6: Velocity Profile in Poiseuille Flow (from La Barck Jr. et al. 2010)

The transmissibility relation as shown above is derived by assuming Poiseuille flow in the bonds. The transmissibility for all the bonds in the network is computed and the set of equations (Equation (1.2)) are solved for the pore network. The pressures at

each of the nodes present in the network are computed by solving the set of equations (Equation 1.2) for all the nodes. From these pressure values, a flow rate ($q_{steadystate}$) in the sample can be determined assuming incompressible flow. This flow rate combined with other parameters like cross-sectional area (A) of the entire pore network, distance (L) between two opposite planes and pressure gradient ($\Delta p_{Steadystate}$) across the two opposite planes help us to determine an average value of permeability (k) using Darcy's equation (Equation (1.4)).

$$k = \frac{q_{steadystate}\mu L}{A\Delta p_{Steadystate}} \tag{1.4}$$

This method is repeated for other planar directions and a permeability value is obtained for all the three planar directions. The planar permeability in Y-direction is higher than the other two direction planar permeability values by about 300-400 md (Table 2).

Pressure Gradient Direction	**Permeability (md)**
Z	1219
X	1367
Y	1682

Table 2: Steady State Permeability Results from the Carbonate Sample (Pasumarti, 2014)

1.2 Pressure Transient Analysis

Pressure Transient Analysis (PTA) is a well-studied topic in the field of petroleum engineering (Lee, Rollins, Spivey, 2003). The analysis involves the study of the pressure waves or transients that are moving through the reservoir. The pressure at any point in the reservoir is computed by solving the diffusivity equation.

$$\frac{1}{r}\frac{\partial}{\partial r}\left(r\frac{\partial p}{\partial r}\right) = \frac{\phi\mu c_t}{k}\frac{\partial p}{\partial t} \tag{1.5}$$

Equation (1.5) is the diffusivity equation and this is used to calculate pressure for flow through porous media.

$$\lim_{t\to 0} p(r,t) = p_i \tag{1.6}$$

The Equation (1.6) represents the initial condition in the reservoir. The pressure is assumed to be the same throughout the reservoir initially.

$$\lim_{r\to 0}\left(\frac{2\pi rhk}{\mu}\frac{\partial p}{\partial r}\right) = q_{source/sink} \tag{1.7}$$

The Equation (1.7) represents the boundary condition at the well.

$$\lim_{r\to \infty}\left(r\frac{\partial p}{\partial r}\right) = 0 \tag{1.8}$$

$$\lim_{r\to \infty} p(r,t) = p_i \tag{1.9}$$

The Equation (1.8) represents the no-flow boundary condition and the Equation (1.9) represents the constant pressure boundary condition.

The diffusivity equation is solved subject to the boundary conditions shown above. This is called the line source solution. An expression of the pressure obtained

from a line source solution is shown in Equation (1.10). The line source solution is valid for an infinite reservoir.

$$p(r,t) = p_i - \frac{q_{line}\mu B}{4\pi kh} E_1\left(\frac{\phi\mu c_t r^2}{4kt}\right) \tag{1.10}$$

The main advantage of pressure transient analysis is to characterize a reservoir. This method is popularly known as the well test derivative analysis (Bourdet, 1989). The plot of the well test derivative (t*dp/dt) vs time (t) on a log-log scale will give various shapes depending upon the flow regime. The top curve is the drawdown vs time and the bottom curve is the well test derivative vs time in Figure 7. We can see a flat trend in the well test derivative curve which is indicative of a radial flow regime or also known as Infinite Acting Radial Flow (IARF).

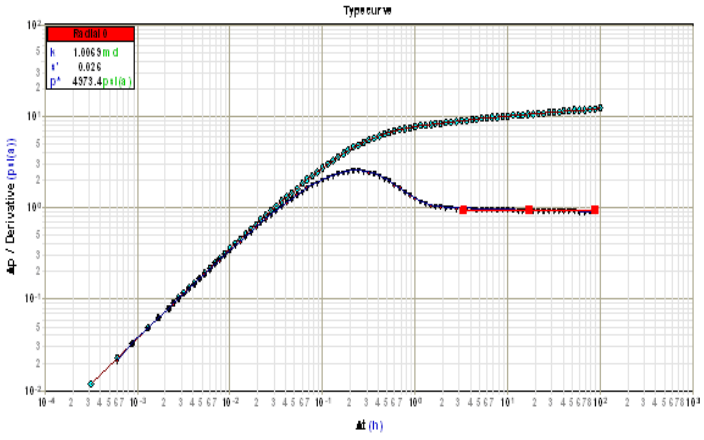

Figure 7: Well Test Derivative vs Time for Infinite Acting Radial Flow (Courtesy Fekete Harmony and Fekete Website)

The magnitude of the well test derivative in the flat portion is used to calculate the permeability of the reservoir. This method is described below.

$$p_i = p_{wf} + \frac{q_{line}\mu B}{4\pi kh} ln(\frac{4kt}{\phi\mu c_t r_w^2 \gamma}) \quad (1.11)$$

Equation (1.11) is the log approximation for Equation (1.10) for $\frac{kt}{\phi\mu c_t r_w^2} > 25$. Here, γ is the Euler constant equal to 1.781. Equation (1.11) can be converted to a form shown in Equation (1.12).

$$p_i - p_{wf} = m * ln(t) + c \quad (1.12)$$

$$m = \frac{q_{line}\mu B}{4\pi kh} \quad (1.13)$$

Equation (1.14) can be obtained by differentiating Equation (1.12) with time.

$$t\frac{d(p_i - p_{wf})}{dt} = m \quad (1.14)$$

Equation (1.14) can be derived from Equation (1.12). Equation (1.14) shows that the well test derivative is constant for the IARF flow regime. The value of the constant well test derivative in the plot Figure 7 can be used to determine permeability.

$$k = \frac{q_{line}\mu B}{4\pi m_{rf} h} \quad (1.15)$$

m_{rf} in Equation (1.15) is the value of the constant well test derivative representing IARF (Figure 8).

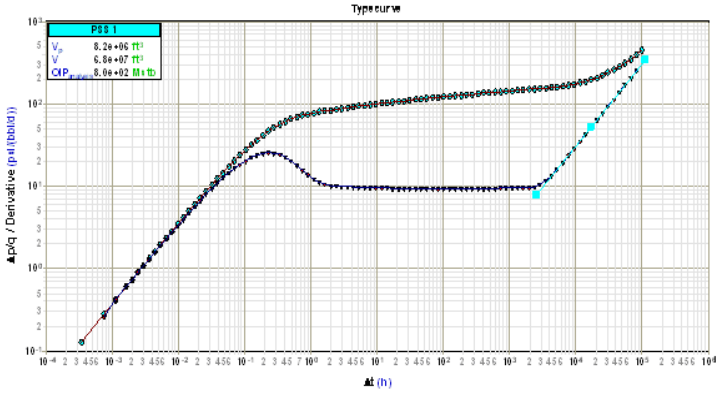

Figure 8: Well Test Derivative vs Time for Finite Size Reservoir (Courtesy Fekete Harmony and Fekete Website)

The top curve is the drawdown vs time and the bottom curve is the well test derivative vs time on a log-log scale in Figure 8. The well test derivative shows a flat trend and a unit slope at later time values. The unit slope is due to the interaction of the pressure transient with reservoir boundaries in a finite sized reservoir. The value of the slope can be used to get an estimate of the permeability of the reservoir.

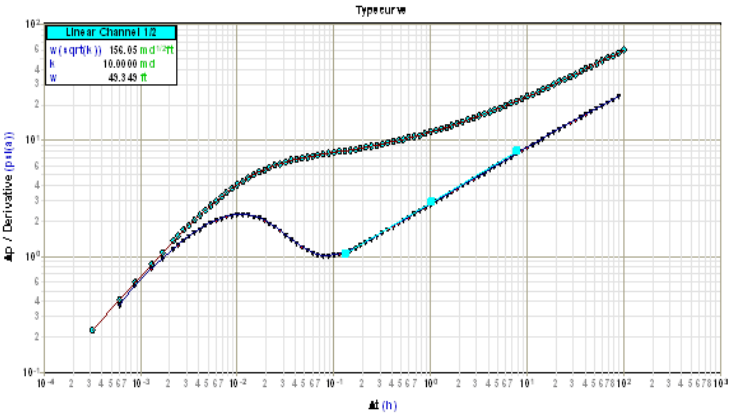

Figure 9: Well Test Derivative vs Time for Linear Flow (Courtesy Fekete Harmony and Fekete Website)

The top curve is the drawdown vs time and the bottom curve is the well test derivative vs time on a log-log scale in Figure 9. The well test derivative shows a 1/2 slope. This is indicative of a linear flow regime seen in fractures or channelized reservoirs.

An important point to note in all these derivative plots is that the drawdown vs time plot doesn't provide any useful insight into the type of flow regime whereas the derivative plot can clearly distinguish between flow regimes.

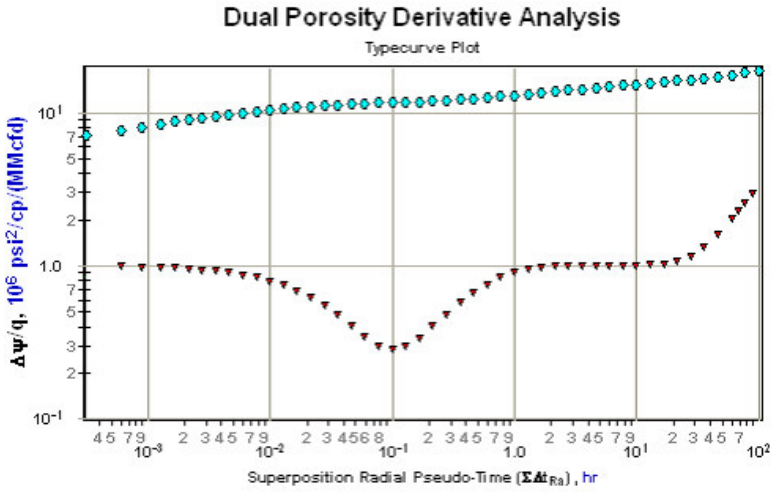

Figure 10: Well Test Derivative vs Time Plot for Dual Porosity Reservoir (Courtesy Fekete Harmony and Fekete Website)

The well test derivative response can also be used to characterize the type of reservoir. The bottom plot in Figure 10 is the well test derivative plot. We can see a decrease and increase in the derivative. This sort of behavior is characteristic of a dual porosity reservoir. This response can be analyzed using analytical methods to estimate

various parameters related to the reservoir. This method related to dual porosity reservoirs will be discussed further in detail later (Section-2.3.2).

1.3 Dijkstra and Fast Marching Methods

Dijkstra (after Dijkstra, 1959) and Fast Marching Methods (FMM) (after Sethian, 1999) are commonly used methods to solve the Eikonal equation on a set of nodes or a graph. The FMM method is the generalization of the Dijkstra algorithm for a multidimensional grid.

Dijkstra's method has been used for analysis shown in the thesis. This is due to the fact that we have used a lattice type framework to represent the carbonate and synthetic sandstone framework. Dijkstra's algorithm is the only algorithm that can be used for a lattice type framework. The characteristic and the gradient of DTOF (Diffusive Time of Flight) is perfectly aligned in such frameworks and so there is no problem of causality (Zhang et.al, 2013) if Dijkstra's algorithm is used. The multidimensional grid solved using Dijkstra and FMM methods gives very close solutions if the permeability field is heterogeneous (described in detail in Sec 2.1.1, Figure 17). The FMM solution will be shown to be more accurate and closer to the actual solution for a homogeneous case (Figure 16). Since the pore network is highly heterogeneous, the Dijkstra algorithm would therefore be close to the actual solution even though we are not using the FMM method (Figure 17).

The FMM is more amenable to continuous frameworks such as reservoir simulation grids. Each cell center or cell vertex in the simulation grid is represented as a node. The nodes are connected to each other. The solution of the FMM gives Diffusive

Time of Flight (DTOF) values for all the nodes. The DTOF gradient is not necessarily along the direction in which nodes are connected as opposed to the Dijkstra method. This is more realistic since pressure waves travel in all directions.

Both Dijkstra and FMM methods are computationally fast and extremely cheap. In our case, the Dijkstra's method was used to do computations on an 83000 node network on a 32/64 bit desktop computer. Every computation on the complete network took around 2 -3 minutes.

1.4 Proposed Solution Methods

We have used two different methods to analyze the synthetic sandstone and the carbonate pore network. Both of these methods are rooted in the pressure transient methodology.

The first method that we have used makes use of the well test derivative response that is calculated based on the DTOF computation that is performed on the pore network. This simulated well test derivative is compared and fitted with an analytical well test derivative. This analytical well test derivative is based on the principles of dual porosity (Warren and Root, 1963). The parameters in the analytical model are varied to determine the best fit possible. These parameters provide an estimate of permeability and other transport parameters (Warren and Root, 1963).

The second method that has been used in this work is based upon the Depth of Investigation (DOI) principle. The pressure derivative reaches a maximum value at different time values at different points in space. The distance at which the pressure derivative has reached a maximum value at a particular time is called the DOI at that

particular time. A particular plane is chosen in the pore network and the time at which that particular plane becomes the DOI for our chosen source is used to calculate permeability for the pore network.

2. TRANSIENT METHODOLOGY

Until now we have discussed methods which incorporate the steady state methodology for the determination of permeability and other transport parameters. But the steady state methodology may not be able to capture the effects of different types of porosity in carbonate rocks. This is due to the fact that the carbonate rocks have different types of porosity which work in conjunction to contribute towards flow in the reservoir. A transient methodology can capture the effect of the heterogeneities of porosity and connectivity in a rock formation.

The steady state method gives an average estimate of the parameters of the rock type being examined. In contrast, the transient method gives a good understanding of the interaction of the heterogeneity present in the model. This method was used to get a quantitative understanding of the parameters like permeability in carbonate rocks. The transient method is useful in gaining an insight in to the type of flow regime that exists in the sample. The permeability determined from transient method is more representative since steady state incompressible flow doesn't occur frequently in a reservoir.

The steady state method involves large computations involving inversion of big matrices. The transient method that was used in our research doesn't involve any intensive computation since the Dijkstra method scales as O (NlogN) where N is the number of nodes (Dijkstra, 1959). Therefore, we are able to do much more computations over a large range of time interval.

2.1 Diffusive Time of Flight

Diffusive Time of Flight (DTOF) is a concept that has its roots in the radius of investigation concept. A radius of investigation (ROI) is defined as the distance of peak pressure disturbance from an impulse source or sinks (Lee, 1982). The following equation shows the method of calculating ROI. It is obtained by equating the double derivative of the pressure (Eqn-1.10) with respect to time to zero. The derivation for the ROI is shown in detail in Section 2.1.3.

$$r_{inv,radial} = \sqrt{\frac{4kt}{\phi \mu c_t}} \tag{2.1}$$

The radius of investigation is the distance from the source at which the rate of pressure change is maximum. This distance keeps increasing with time as shown in Figure 11. We can see that the pressure keeps on decreasing at the wellbore. The distance from the wellbore at which the pressure starts to decrease increases with time. This is the distance at which rate of pressure change will be maximum (Equation (2.1)) and it increases with time.

The limitation with above concept is that it is only applicable to 2D homogeneous permeability fields (Lee, 1982). Therefore the concept of Diffusive Time of Flight (DTOF) was developed to apply it to heterogeneous permeability fields (Kulkarni et al. 2000).

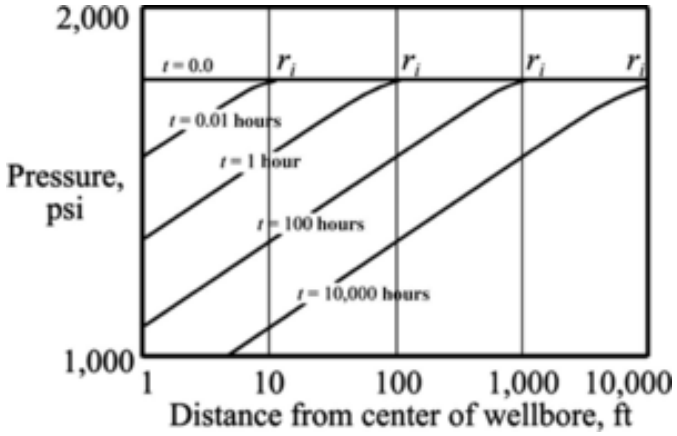

Figure 11: Radius of Investigation (Lee, 1982)

The diffusivity equation is converted from the time domain to frequency domain by using a Fourier transform. Then the pressure is expanded in an asymptotic form and the low frequency terms are neglected. The high frequency term represents the sharpest pressure wave front in the reservoir. Subsequently, the Eikonal equation is obtained which is shown below.

$$\sqrt{\alpha(\vec{x})}|\nabla\tau(\vec{x})| = 1 \tag{2.2}$$

$$\tau = \sqrt{\frac{\phi\mu c_t}{k}} * r \qquad \alpha = \frac{k}{\phi\mu c_t} \tag{2.3}$$

The Equation (2.2) is the Eikonal equation. α is known as diffusivity.τ is the DTOF and r is the distance. The DTOF in Equation (2.3) is valid for 1-D discretization. The DTOF (τ) captures the heterogeneities of permeability, porosity and compressibility present in the reservoir. DTOF acts as a spatial co-ordinate.

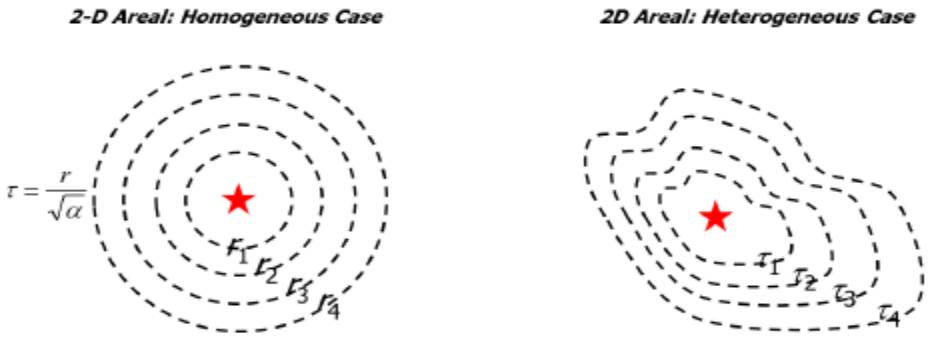

Figure 12: Diffusive Time of Flight Contours for Homogeneous and Heterogeneous Permeability Fields ($\tau_1 < \tau_2 < \tau_3 < \tau_4$) (Pasumarti, 2014)

Figure 12 shows the propagation of DTOF in homogeneous and heterogeneous permeability fields, which in effect shows the pressure wave transmission direction. The DTOF is increasing radially uniformly for the homogeneous permeability field. In the case of the heterogeneous permeability field, the DTOF contours are more widely spaced in one direction as compared to other directions. This effect is occurring due to the presence of high permeability in that direction. Therefore, the pressure wave will travel faster in the direction of higher permeability.

2.1.1 Dijkstra's Method

The Dijkstra's method is used to compute the DTOF for the complete pore network model in our research. It is based on a single pass approach and is has a running time of O (NlogN) where N is the number of nodes .This method is a very common algorithm used to find the shortest path between nodes on a graph (Dijkstra, 1959). In our case we are using this algorithm to compute the global DTOF for all the nodes in the

pore network. This method works because the fastest pressure wave will always take the path which has the least DTOF among all available paths.

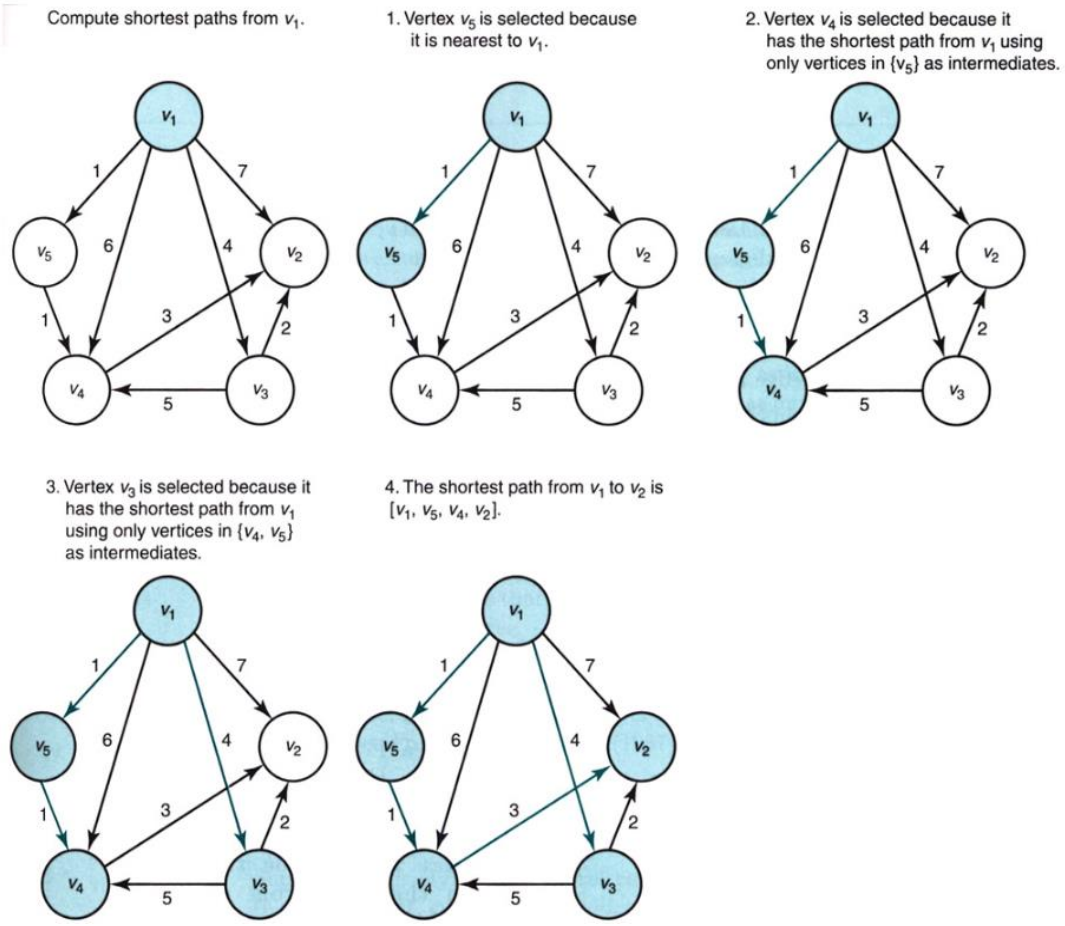

Figure 13: Diagrammatic Representation of Dijkstra's Method (Neapolitan, 2011)

Here we provide an explanation of the Dijkstra's method. The nodes shown are the nodes in a pore network model. The bonds connecting the nodes have a value of DTOF assigned to them. This DTOF is computed using the Equation (2.4).

$$\tau_{bond} = \sqrt{\frac{\phi \mu c_t}{k_{bond}}} * L_{bond} \tag{2.4}$$

The Equation (2.4) is the solution of the Eikonal equation along a 1-D lattice bond. We start the simulation at a particular node or a set of nodes which are be referred to as seed nodes with a DTOF of zero. These nodes are assigned to a set called SELECTED NODES.

The nodes other than these seed nodes are initially assigned a DTOF value of infinity. The neighboring nodes to these seed nodes are determined and are assigned to a set called NEIGHBOR NODES. The node which has the least DTOF among these neighboring nodes is chosen as the next selected node. The DTOF of the selected nodes are assigned as per the following relation.

$$\tau_{selected\ node} = \tau_{previous\ node} + DTOF\ of\ the\ bond\ from\ previous\ node\ to\ selected\ node \tag{2.5}$$

The selected node and its corresponding DTOF is assigned to the set of SELECTED NODES. This selected node is removed from the NEIGHBOR set. The DTOF values for the new set of neighbor nodes for the currently selected node is computed and these new neighbor nodes are assigned to the NEIGHBOR NODES set. The node with the minimum value of DTOF in the NEIGHBOR Node set becomes the new selected node. It is then removed from the NEIGHBOR set and put into the SELECTED set. This process is continued until all the nodes have been populated.

Dijkstra's algorithm has a grid orientation effect (Figure 14). Figure 14 shows four equidimensional cells with constant values of ϕ, μ, c_t and k throughout the grid. This means that DTOF is only a function of distance (Equation (2.4)). In a Dijkstra algorithm if simulation starts from cell/node-1, then the DTOF of cell/node-3 will be $2\Delta\tau_1$ since $\Delta\tau_1$ is equal to $\Delta\tau_2$ and the path followed by Dijkstra will be from cell/node1 to cell/node-3 via cell/node-2. The actual DTOF for cell/node-3 is$\Delta\tau_3$. The length of the path 1-2-3 is $\sqrt{2}$ times the length of the path1-3. Therefore, the Dijkstra based DTOF for cell/node-3 ($2\Delta\tau_1$) will be $\sqrt{2}$ times the actual DTOF ($\Delta\tau_3$) since the DTOF is only a function of distance on a homogeneous grid.

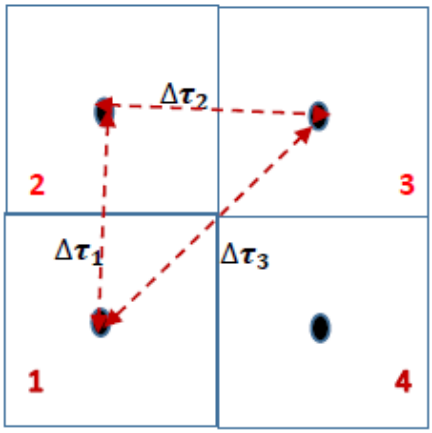

Figure 14: Dijkstra DTOF Calculation on a Grid

We will now describe the DTOF calculation by FMM on a grid (Figure 15). Figure 15 shows four equidimensional cells. We are attempting to calculate the DTOF for cell (i,j). Eikonal equation (Equation (2.2)) is discretized as shown in Equation (2.6)

for the FMM method on a grid where $\tau_{i,j}$ is the DTOF for the cell (i,j) (Zhang et al. 2013).

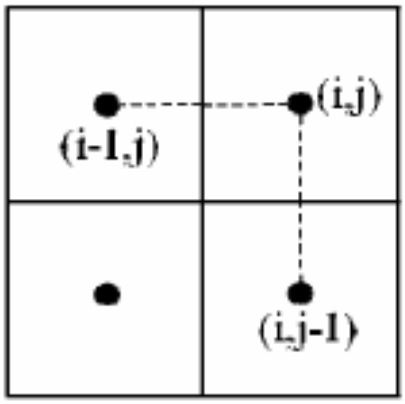

Figure 15: FMM DTOF Calculation on a Grid (Zhang et al. 2013)

$$(\tau_{i,j} - \tau_{i,j-1})^2 + (\tau_{i,j} - \tau_{i-1,j})^2 = \frac{\phi \mu c_t}{k} * \Delta x^2 \tag{2.6}$$

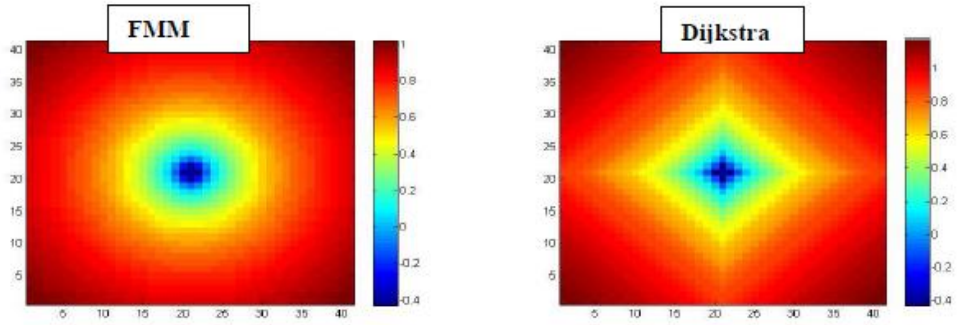

Figure 16: Diffusive Time of Flight Comparison for Homogeneous Permeability Field between Dijkstra and Fast Marching Method (Pasumarti, 2014)

We will now compare the performance of Dijkstra and FMM method on a homogeneous and a heterogeneous grid. Figure 16 shows that there is a considerable difference in the DTOF computed by the Dijkstra and the FMM method for homogeneous fields on a grid due to grid orientation effect in Dijkstra's algorithm. The grid orientation effect can easily be seen in Dijkstra based DTOF. The DTOF along the diagonals are higher than along the edges because of the reasons mentioned previously.

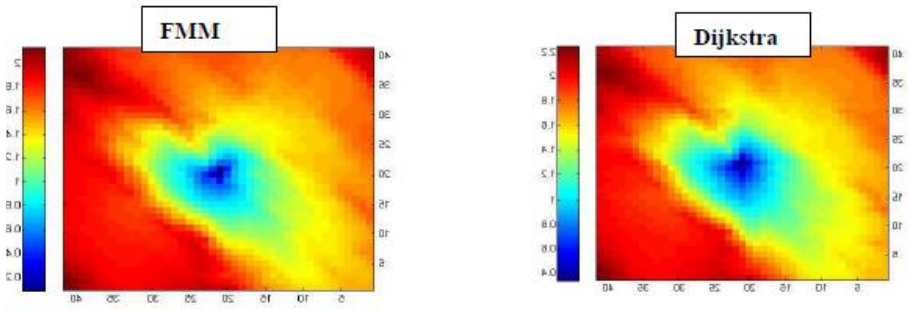

Figure 17: Diffusive Time of Flight Comparison for Heterogeneous Permeability Field between Dijkstra and Fast Marching Method (Pasumarti, 2014)

Figure 17 shows that the DTOF computed by Dijkstra and FMM are almost same when there is a heterogeneous permeability field on a grid. Heterogeneity is dominating over grid orientation effect.

We will be solving for DTOF on a pore network for which we will be using the Dijkstra algorithm. Equation (2.6) shows that gradient of DTOF for cell (i, j) is discretized along two neighboring perpendicular components. Therefore, the DTOF gradient vector ($\nabla\tau(\vec{x})$) will be aligned somewhere between the two perpendicular

components of the DTOF gradient vector. This makes sense on a grid because pressure transmits in all directions. On a pore network, it doesn't make sense if the DTOF gradient vector is between the bond directions because there is no pressure transmission in between the bonds.

2.1.2 Drainage Volume, Well Test Derivative and Depth of Investigation

As the simulation proceeds, more nodes are drained. The drainage volume at any point of time is derived from an asymptotic approximation (Zhou et.al. 2013). To relate the drainage volume to DTOF and time, we need to start from the radial diffusivity equation given as follows.

$$\frac{1}{A(r)}\frac{\partial}{\partial r}\left(\frac{k}{\mu}A(r)\frac{\partial p(r,t)}{\partial r}\right) = \phi c_t \frac{\partial p}{\partial t} \tag{2.7}$$

The flux is given by the following equation.

$$q(r,t) = \frac{kA(r)}{\mu}\frac{\partial p(r,t)}{\partial r} \tag{2.8}$$

By using the Equation (2.6) and (2.7) we get the following relation.

$$c_t \frac{\partial p}{\partial t} = -\frac{1}{\phi A(r)}\frac{\partial q}{\partial r} = -\frac{\partial q}{\partial V_p(r)} \tag{2.9}$$

The above equation is for a regular homogeneous co-ordinate system in terms of 'r'. We have already shown the relation between DTOF (τ) and radius (r). Therefore we will express these equations in terms of DTOF.

$$c_t \frac{\partial p}{\partial t} = -\frac{\partial q}{\partial V_p(\tau)} \tag{2.10}$$

The geometric approximation (Xie et al. 2012) is applied to Equation (2.10) by the following relation.

$$c_t \frac{\partial p}{\partial t} = -\frac{q_{line}}{V(t)} \tag{2.11}$$

The Equation (2.11) is valid only at the wellbore.

$V(t)$ is the drainage volume at a particular time for the complete system. An improved version (Zhou et al. 2013) of this geometric approximation known as asymptotic approximation (Equation (2.12)). Equation (2.12) is valid at all locations in the reservoir.

$$c_t \frac{\partial p}{\partial t} = -\frac{\partial q}{\partial V_p(\tau)} = -\frac{q_{line}}{V(t)} e^{-\frac{\tau^2}{4t}} \tag{2.12}$$

On integrating Equation (2.12) from a finite volume $V_p(\tau)$ with a flux $q(\tau, t)$ to an infinite volume and a corresponding flux of zero gives the following relation.

$$q(\tau, t) = \frac{q_{line}}{V(t)} \int_{V_p(\tau)}^{\infty} dV_p(\tau) e^{-\frac{\tau^2}{4t}} \tag{2.13}$$

The boundary condition at the wellbore is q=q_w for $V_p(\tau) = 0$. Using the Boundary condition, the following relation is derived.

$$V(t) = \int_0^{\infty} dV_p(\tau) e^{-\frac{\tau^2}{4t}} \tag{2.14}$$

The above equation can be written in discrete form as the following equation.

$$V(t) \cong \sum_j PV_j e^{-\frac{{\tau_j}^2}{4t}} \tag{2.15}$$

The Equation (2.15) can be used to find the drainage volume as a function of time when the DTOF values for all the nodes are known. Figure 18 shows how the drainage volume from the simulation increases with time.

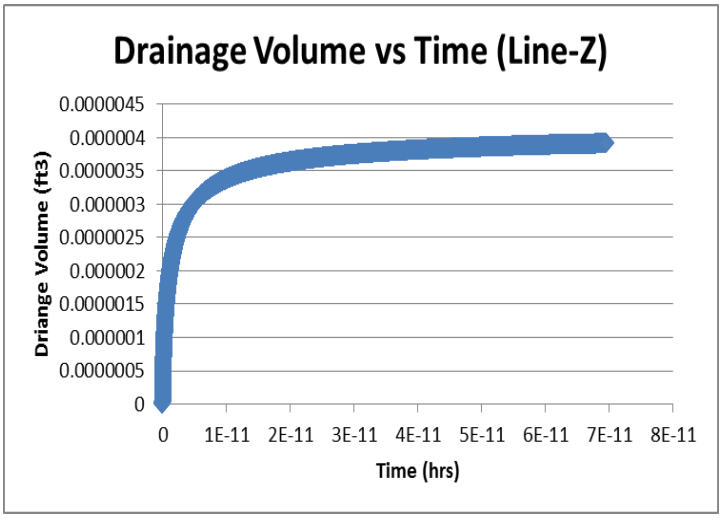

Figure 18: Drainage Volume vs Time Plot Obtained from Simulation

$$t\frac{\partial p}{\partial t} = -\frac{q_{line}t}{c_t V(t)} \tag{2.16}$$

Equation (2.16) is used to compute the Well Test Derivative (WTD) at the wellbore or at the seed nodes in the pore network. The seed nodes chosen for simulation to calculate the well test derivative are at the center of the pore network (Figure 19).

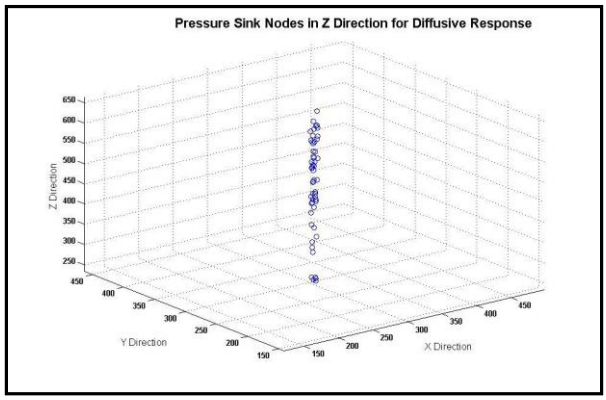

Figure 19: Seed Nodes in Line-Z Direction (Pasumarti, 2014)

The seed nodes are aligned in Line-Z, Line-X and Line-Y direction at the center of the pore network. These seed nodes act like a well or a line source at the center of the pore network. The DTOF values at these seed nodes are zero since these are the nodes from which the simulation starts. Therefore the Well Test Derivative (WTD) at these seed nodes is given by Equation (2.16).

Now, we will derive a relation for Depth of Investigation (DOI) (Pasumarti, 2014). The Depth of Investigation is defined as the distance from the source at which the pressure derivative ($\frac{\partial p}{\partial t}$) is maximum. If the pressure derivative is maximum the double derivative will be zero (Equation (2.17)).

$$\frac{\partial^2 p}{\partial t^2} = 0 \tag{2.17}$$

Equation (2.16) and Equation (2.17) is used to get Equation (2.18).

$$\left(-\frac{1}{V(t)^2}\frac{dV(t)}{dt} + \frac{1}{V(t)}\frac{\tau^2}{4t}\right)e^{-\frac{\tau^2}{4t}} = 0 \tag{2.18}$$

Equation (2.19) is obtained from Equation (2.14).

$$\frac{dV(t)}{dt} = \int_0^\infty \frac{\tau^2}{4t} dV_p(\tau) e^{-\frac{\tau^2}{4t}} \tag{2.19}$$

Equation (2.19) is substituted in Equation (2.18). Since, the exponential term in Equation (2.18) can't be zero, the expression inside the bracket in Equation (2.18) is equated to zero in Equation (2.20).

$$\tau^2(t) = \frac{1}{V(t)} \int_0^\infty \tau^2 dV_p(\tau) e^{-\frac{\tau^2}{4t}} = \frac{\int_0^\infty \tau^2 dV_p(\tau) e^{-\frac{\tau^2}{4t}}}{\int_0^\infty dV_p(\tau) e^{-\frac{\tau^2}{4t}}} \tag{2.20}$$

Equation (2.20) is a general expression for DOI ($\tau^2(t)$) as a function of time.

$$\tau^2(t) \approx \frac{\sum_{j=1}^{N} {\tau_j}^2 PV_j e^{-\frac{{\tau_j}^2}{4t}}}{\sum_{j=1}^{N} PV_j e^{-\frac{{\tau_j}^2}{4t}}} \tag{2.21}$$

Equation (2.21) is an expression for DOI in a pore network where N is the number of nodes, PV_j is the volume of the jth node and τ_j is the DTOF of the jth node.

For a linear flow, Equation (2.22) gives the pore volume ($V_p(r)$) with distance where r is the linear distance from the source and A is the cross-sectional area to flow.

$$V_p(r) = rA\phi \tag{2.22}$$

Equation (2.23) gives the DTOF (τ) for a linear flow.

$$\tau = \sqrt{\frac{\phi \mu c_t}{k}} r \tag{2.23}$$

Equation (2.22) and Equation (2.23) can be used to get Equation (2.24).

$$dV_p = \sqrt{\frac{k}{\emptyset \mu c_t}} A \emptyset d\tau \tag{2.24}$$

Equation (2.20) can be converted for use in a finite domain where τ_{max} is the maximum DTOF in the finite domain.

$$\tau^2(t) = \frac{\int_0^{\tau_{max}} \tau^2 dV_p(\tau) e^{-\frac{\tau^2}{4t}}}{\int_0^{\tau_{max}} dV_p(\tau) e^{-\frac{\tau^2}{4t}}} \tag{2.25}$$

On simplifying Equation (2.25) using Equation (2.24), we get the following equation.

$$\frac{\tau^2}{4t} = \frac{\sqrt{\pi}\,\mathrm{erf}\left(\frac{\tau_{max}}{2\sqrt{t}}\right) - 2e^{-\frac{{\tau_{max}}^2}{4t}} * \frac{{\tau_{max}}^2}{4t}}{2\sqrt{\pi}\,\mathrm{erf}\left(\frac{\tau_{max}}{2\sqrt{t}}\right)} \tag{2.26}$$

Since τ_{max} is very large, $e^{-\frac{{\tau_{max}}^2}{4t}}$ becomes negligible at finite time (t). Therefore, we get Equation (2.27).

$$\frac{\tau^2}{4t} = \frac{1}{2} \tag{2.27}$$

Equation (2.27) is valid for linear flow. Similar expressions can be derived for radial and spherical flow by using $V_p(r) = cr^2$ and $V_p(r) = cr^3$ respectively. Here, r is the radial distance from source and c is a constant. $\frac{\tau^2}{4t}$ will be equal to 1, 3/2 for radial and spherical flow respectively.

2.2 Dual Porosity

The dual porosity model (Warren and Root, 1963) is used to describe fractured carbonate reservoirs. This model has two components: fractures and matrix. The fractures comprise a very small volume of the rock and store a small amount of fluid.

These fractures provide the pathway for the fluids to flow through the rock. The matrix contains the majority of the pore volume of the rock but these matrix pore spaces are not interconnected and hence do not provide pathways for the fluid to flow. The matrix starts draining into the fractures as soon as fluid starts to flow from the fractures towards the wellbore.

$$\nabla^2 p_{fd} = \omega \frac{\partial P_{fd}}{\partial t_d} - \lambda(p_{md}\text{-}p_{fd}) \tag{2.28}$$

Equation (2.28) is for fracture flow.

$$(1-\omega)\frac{\partial p_{md}}{\partial t_d} = \lambda(p_{md} - p_{fd}) \tag{2.29}$$

Equation (2.29) is for matrix to fracture flow.

$$\lambda = \alpha \frac{k_m}{k_f} r_w^2 \tag{2.30}$$

$$\omega = \frac{(\phi c_t)_f}{(\phi c_t)_f + (\phi c_t)_m} \tag{2.31}$$

There are 2 main parameters in this model. The interporosity flow coefficient (λ) controls the rate of flow from the matrix to the fracture and the storativity ratio (ω) gives the ratio of the fracture to matrix volume.

2.2.1 Dual Porosity Rationale for the Carbonate Network Model

The well test derivative (WTD) plot (Figure 20) is for a set of Line-Z seed nodes in the carbonate pore network. The Line-Z seed nodes act as a line source.

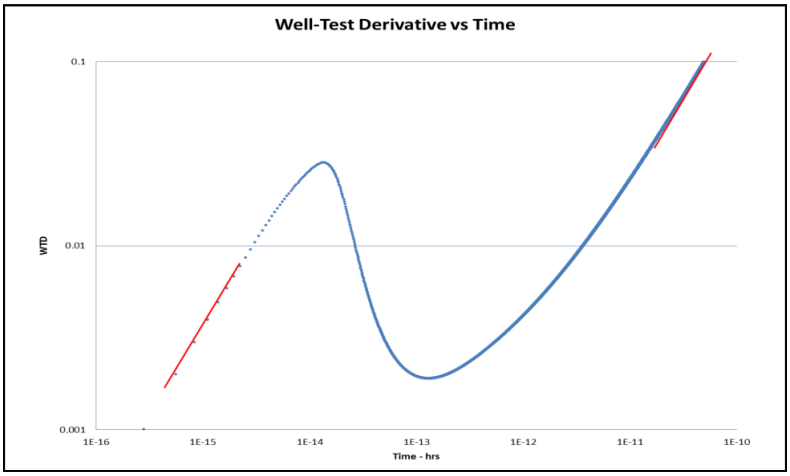

Figure 20: Well Test Derivative vs Time Plot Obtained from Simulation in Carbonate Pore Network (Pasumarti, 2014)

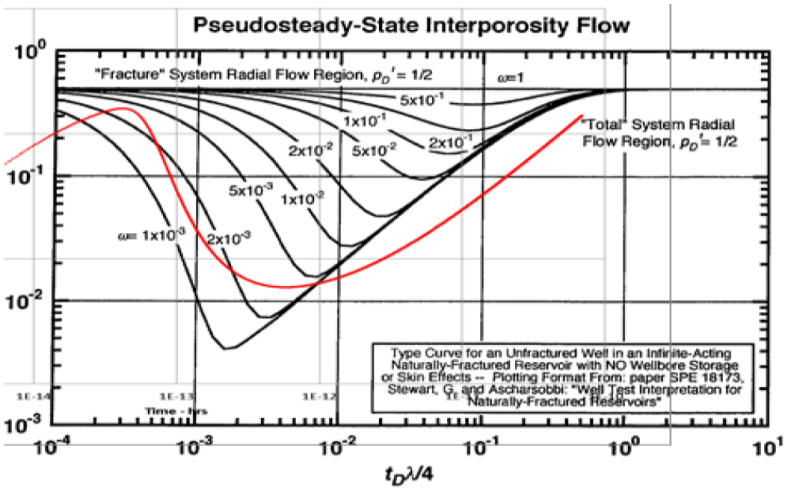

Figure 21: Match of Well Test Derivative from Simulation with the Dual Porosity Type Curve (Pasumarti, 2014)

Figure 21 shows the match of the well test derivative (red curve) with the type curves (black curves). It can be seen that the derivative is having a similar shape as the type curves. This is the reason behind assuming a dual porosity model for the carbonate pore network.

The dual porosity model discussed before includes a small well-connected pore space (fractures) feeding to the well which is in turn connected to a large volume of poorly connected pore space (matrix). This fracture-matrix analogy can be extended to the carbonate rocks at a micro scale. The carbonate rocks have an intra-granular and inter-granular porosity at the pore scale. The inter-granular porosity provides a clear pathway for the fluids to be transported while holding a small part of the total fluid content. On the other hand, the intra-granular porosity contains a large percentage of the fluid content but it is poorly connected. The intra-granular pores feed into the inter-granular pores which provide a pathway for flow to the well.

Reservoir Scale	**Pore Scale**
Matrix pore space	Intra-granular pore space
Fracture pore space	Inter-granular pore space
$\omega = \frac{Fracture\ Pore\ volume}{Total\ Pore\ volume}$	$\omega = \frac{Intergranular\ Pore\ volume}{Total\ Pore\ volume}$
λ- Controls flow from Matrix to Fracture	λ-Controls flow from Intra-granular (Secondary) to Inter-granular (Primary) Pore space

Table 3: Dual Porosity Macro-Scale vs Dual Porosity at Micro-Scale

2.2.2 Well Test Derivative in Dual Porosity Reservoirs

The well test derivative for dual porosity reservoir follows a unique trend as shown in the plots below. Now, we will qualitatively analyze these plots.

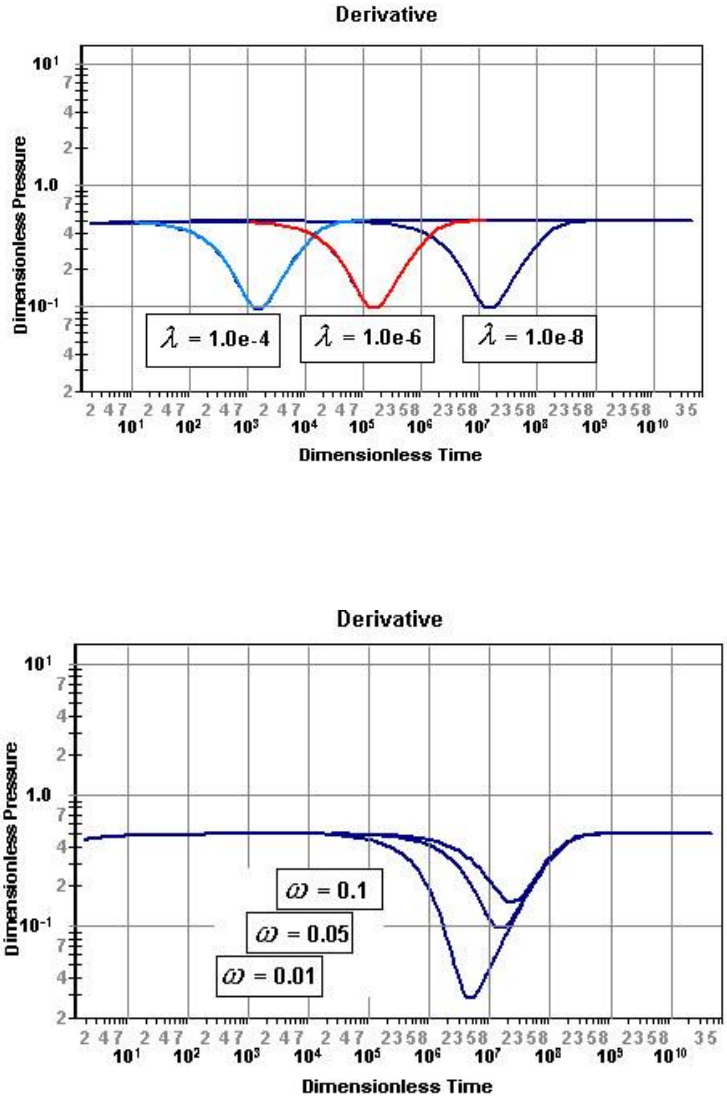

Figure 22: (a) Effect of λ on Well Test Derivative, (b) Effect of ω on Well Test Derivative for a Dual Porosity Reservoir (Lee and Wattenbarger, 1996)

The Figure 22(a) shows the effect of increasing λ on a Well Test Derivative type curve. As λ increases, the decrease in the derivative comes at an earlier time because the matrix responds faster to drawdown. Figure 22(b) shows that as ω decreases, the magnitude of decrease in the derivative increases because of a larger matrix fluid volume. The Well Test Derivative (WTD) in both Figure 22(a) and Figure 22(b) are constant initially. This is due to the fact that the well-connected pore volumes are draining into the well. This flat trend is a signature of the radial flow that exists for a very short amount of time in these well connected volumes (fractures). After this, the Well Test Derivative (WTD) starts to decrease. This decrease in the derivative is due to the flow from the poorly connected pores (matrix) into the fractures. This influx from the matrix gives good pressure support which means that the rate of decline of pressure with time is decreasing. The rate of this influx starts reducing as the pressure difference between the matrix and fracture starts decreasing. Therefore, we can see that the derivative curve starts to rise upwards when the rate of influx from the matrix to the fracture starts to reduce. Finally, the derivative reaches a constant value. This is the point where the matrix and fracture pressures are in equilibrium. At this stage, the flow is infinitely acting radial flow (IARF). This flow regime can be used to estimate the effective fracture permeability of the reservoir.

Storativity ratio (ω) is the parameter that controls the amount of dip in the derivative. The lower the value of the storativity ratio, the higher the magnitude of decrease in the derivative. This is because a low storativity ratio implies higher matrix

volume which means more influx from the matrix to the fractures before the pressure starts to equilibrate.

2.3 Analysis Technique using Well Test Derivative

We will first demonstrate the mehod of analysis of the Well Test Derivative (WTD) curve observed in the synthetic sandstone and then move on to the carbonate pore network dual porosity derivative analysis.

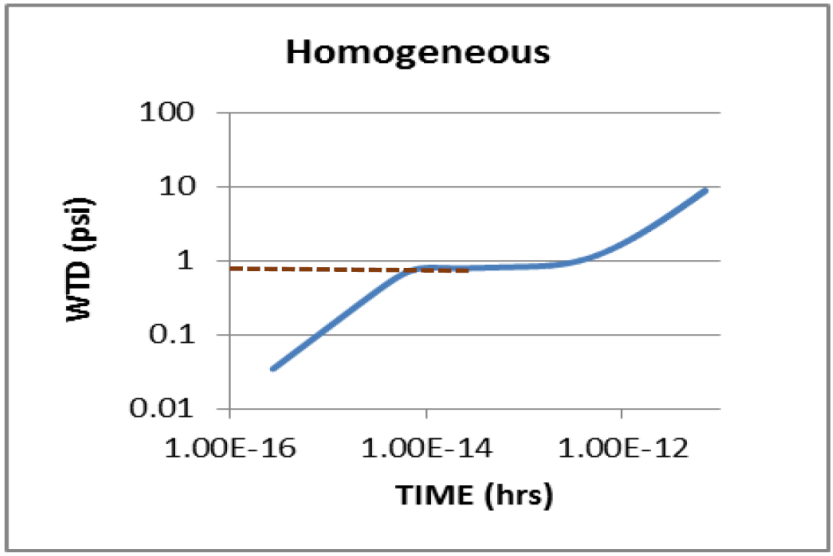

Figure 23: Well Test Derivative Curve for IARF Observed in Synthetic Sandstone

Figure 23 shows the well test derivative (WTD) plot for the synthetic sandstone for a Line-Z seed node simulation. The flat portion in the WTD curve is the IARF flow regime. The IARF region in the WTD can be analyzed to estimate the permeability of the synthetic pore network.

$$k = \frac{q_{line}\mu B}{4\pi m_{rf} h} \tag{2.32}$$

The WTD (m_{rf}) is estimated from the constant well test derivative portion (dashed red line) in the well test derivative plot (Figure 23). The m_{rf} is the value of the constant Well Test Derivative (WTD) for IARF. Equation (2.32) is used to compute the value of permeability (k).

Parameter	**Value**
q_{line}	1 bbl/d
B	1 rb/stb
μ	1.2 cp
h	$5 * 2\sqrt{2} * R_{grain} = 0.00289$ (ft.) (Synthetic Sandstone)

Table 4: Parameter Values for Well Test Derivative Analysis of the Synthetic Sandstone Pore Network. *The values in the table should be used with appropriate conversion factors.*

Now, we will demonstrate the analysis method for the carbonate pore network well test derivative (WTD). It must be noted that an attempt had been made to characterize this carbonate pore network using a dual porosity framework (Pasumarti, 2014). The Stewart and Asharsobbi type curve (black curves in Figure 24) was used to get an estimate of storativity ratio and interporosity flow coefficient from the pore network (Pasumarti, 2014). This method had two problems. The permeability estimated from the steady state technique was required as a starting point in this type curve analysis. Another problem was due to the fact that these type curves are valid for infinite

systems with line source in a dual porosity system. Therefore, these type curves show a constant well test derivative after the matrix and fracture pressure has equilibrated and the flow regime is Infinite Acting Radial Flow (IARF). In our carbonate pore network, the well test derivative doesn't show any IARF region but clearly shows a dual porosity signature.

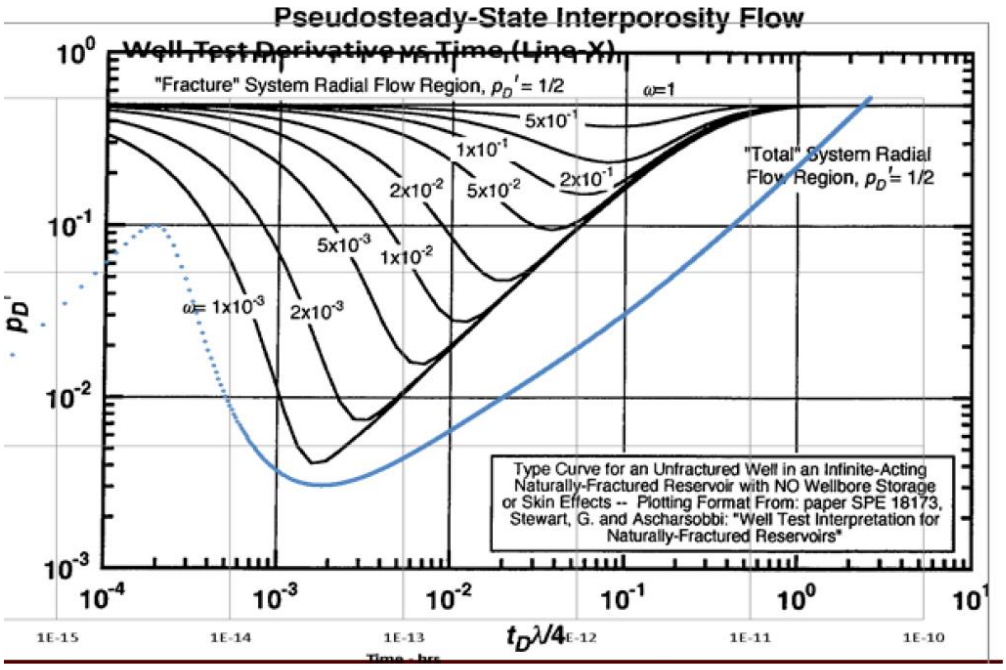

Figure 24: Dual Porosity Type Curve Match with Carbonate Simulation Well Test Derivative Plot (Pasumarti, 2014)

$$\lambda = \frac{4}{\frac{k}{\phi\mu c_t r_w^2}\frac{[t]_{MP}}{[\frac{t_D\lambda}{4}]_{MP}}} \tag{2.33}$$

In Equation (2.33), $[t]_{MP}$ and $[\frac{t_D\lambda}{4}]_{MP}$ are the match points on the well test derivative and the type curve respectively.

Equation (2.33) was used to analyse the well test derivative curve (blue line in Figure 24). A value of permeability (k) was needed for this analysis. Since the well test derivative curve doesn't have any IARF, a value of permeability was not possible to be determined from the derivative curve. Therefore, a permeability value from steady state calculation was used in Equation (2.33) to determine the interporosity flow coefficient (λ) value.

Also for matching the type curve, the IARF region on the well test derivative plot has to be matched properly to get a good estimate. However, we don't observe any IARF in the well test derivative plots in the carbonate pore network. Hence, we decided to use an analytical model to match the derivative from simulation.

Figure 25 shown below is the well test derivative generated from simulation in the carbonate pore network model. We determine the value of ω from this plot. The well test derivative increases to a certain time on this plot. This is the time up to which only the well connected pores (inter-granular pore spaces) are contributing. At a certain time, the well test derivative starts to dip. This is the time at which the secondary pores (intra-granular pore spaces) start contributing to the flow. So we need to find the volume of pores that were contributing to the flow just at the point in time where the well test

derivative starts to decrease. The volume at the end of simulation when the well test derivative has a unit slope, implying that the system has entered Pseudo Steady State (PSS) regime, is the total volume of all the pores.

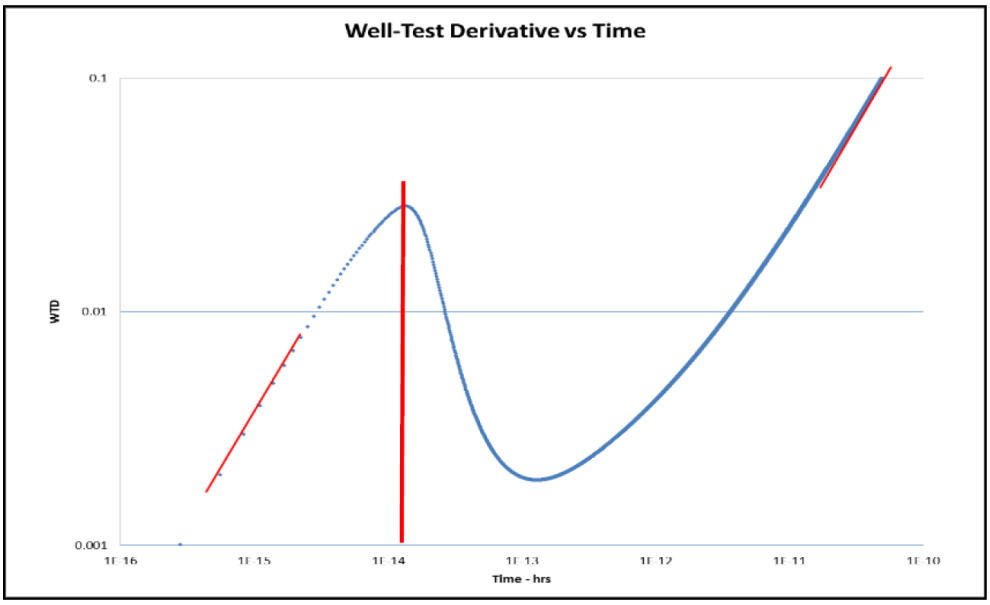

Figure 25: Well Test Derivative in the Carbonate Pore Network for Line-Z Seed Nodes (Pasumarti, 2014)

We now know the volume of the integranular pore space and the total pore space. We can use the following relation to compute the value of the storativity ratio. This method to calculate storativity ratio was shown previously (Pasumarti, 2014).

$$\omega = \frac{Intergranular\ Pore\ volume}{Total\ Pore\ volume}$$

There is a well established analytical model for dual porosity in an infinite reservoir for a line source (Warren and Root, 1963). The following equation gives the relation for the well test derivative for such a model.

$$t_d \frac{\partial p_{fd}}{\partial t_d} = 1/2\{1 - exp(-\frac{\lambda t_d}{(1-\omega)}) + exp\left(-\frac{\lambda t_d}{\omega(1-\omega)}\right)\} \quad (2.34)$$

$$t_d = \frac{k_{fb}t}{(\phi c_t)_t \mu r_w^2} \ , p_{fd} = \frac{2\pi k_{fb} h(p_i - p_{wf})}{q_{line}\mu B} \quad (2.35)$$

The well test derivative (Equation (2.34)) in its dimensionless form is converted into a dimensional form by using the value of the constants in the model. This analytical well test derivative is plotted vs time on the same graph as the plot of the simulated well test derivative vs time on a log-log scale (Figure 26). The analytical well test derivative is matched with the simulated well test derivative by varying the parameters permeability (k) and interporosity flow co efficient (λ). The storativity ratio is not varied during this matching process since it is a geometrical property and its value was already determined.

The values given in Table 5 was used for performing the well test derivative analysis by fitting the analytical model (Equation (2.34)) with the simulated derivative. The results from this analysis have been presented in the results section for carbonates.

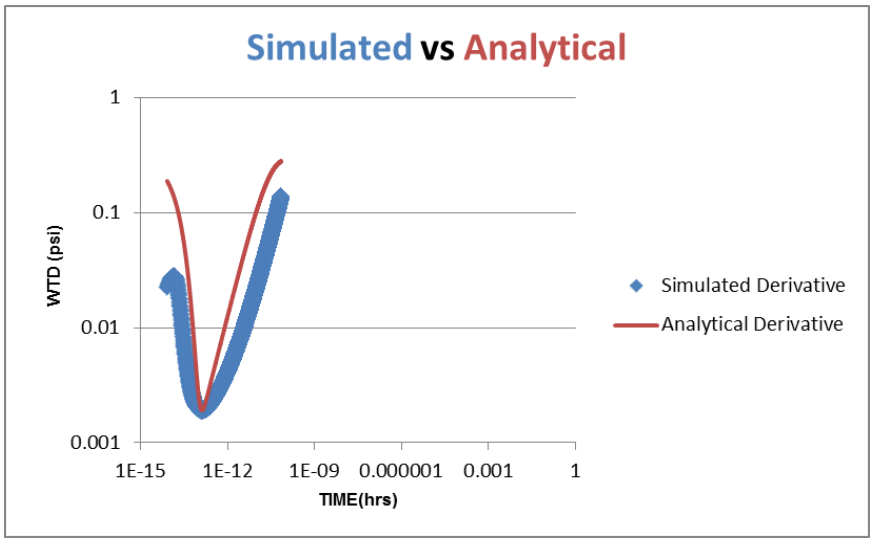

Figure 26: Match of the Simulated and Analytical Well Test Derivative for the Carbonate Pore Network for Line-Z Seed Nodes

Parameter	Value
r_w	2.47E-4, 2.11E-4, 2.81E-4 ft for X, Y,Z directions
μ	0.2 cp
c_t	3e-5 psi^{-1}
ϕ	0.28
q_{line}	1 bbl/d

Table 5: Parameter Values for Well Test Derivative Analysis of the Carbonate Pore Network. *The values in the table should be used with appropriate conversion factors.*

2.4 Analysis Technique using Depth of Investigation

Depth of Investigation (DOI) is a concept which is a generalization of the radius of investigation (Lee, 1982). Depth of Investigation (DOI) is the distance from the initial source/sink at where the pressure derivative ($\frac{\partial p}{\partial t}$) is maximum.

For linear flow we obtain the following equation.

$$r_{inv,linear} = \sqrt{\frac{2kt}{\phi \mu c_t}} \tag{2.36}$$

The Equation (2.36) gives the Depth of Investigation (DOI) at any particular time for a linear flow. Equation (2.36) was derived from Equation (2.23) and Equation (2.27).

The seed nodes for DOI analysis are chosen on a particular plane (Figure 27). The simulations have been repeated for all set of possible seed node (Bottom-XY, Front - XZ, Left -YZ planes) planes for the carbonate pore network. The simulation in the synthetic sandstone network has only been done for the Bottom-XY plane since the model is cubical in shape and the heterogeneities introduced are random and non-directional in nature.

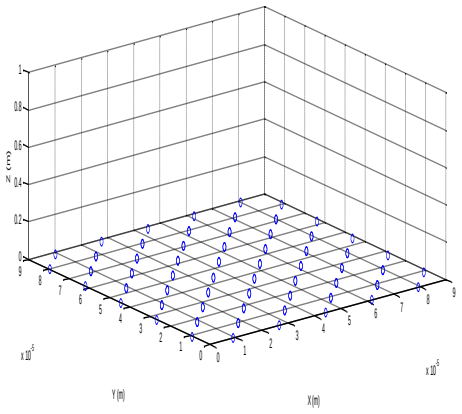

Figure 27: Bottom XY Plane Seed Nodes

We will now derive the drainage volume with time for a planar source in a cuboidal sample (This derivation has been done by Chen Li (TAMU Petroleum Engg. PhD student) but hasn't been published yet). Based on the asymptotic approximation of the diffusivity equation and the association of pressure wave front propagation with τ, we can relate drainage volume as a function of time with drainage volume as a function of DTOF.

$$V(t) = \int_0^\infty dV_P(\tau) \cdot e^{-\tau^2/4t} \tag{2.37}$$

A constant form of $w(\tau)$ is assumed to be present as in Equation (2.38)

$$w(\tau) = \frac{dV_p(\tau)}{d\tau} = \frac{PV}{\tau_{\max} - \tau_{\min}} \tag{2.38}$$

where PV represents the pore volume of the complete network. $\tau_{\min}$ and $\tau_{\max}$ stands for the maximum and minimum DTOF values. $\tau_{\min}$ would be zero for a planar source.

$$dV_p(\tau) = \frac{PV}{\tau_{j,\max} - \tau_{f,\min}} d\tau \tag{2.39}$$

Hence drainage volume as a function of time is given by Equation (2.40).

$$V(t) = \sqrt{\pi t}\left(\frac{PV}{\tau_{max} - \tau_{min}}\right)\left(\operatorname{erf}\left(\frac{\tau_{max}}{2\sqrt{t}}\right) - \operatorname{erf}\left(\frac{\tau_{min}}{2\sqrt{t}}\right)\right) \tag{2.40}$$

The Figure 28 shows the plot of V(t)/$\sqrt{t}$ vs time for arbitrary values of Pore volume (PV) and τ_{max} and time (t) using Equation (2.40). We can see that the quantity V(t)/$\sqrt{t}$ is constant initially and starts to decrease after a certain time. This is the time when all the volume has been drained and V(t) almost becomes a constant. The pressure transient has reached the plane opposite to the source plane at this time.

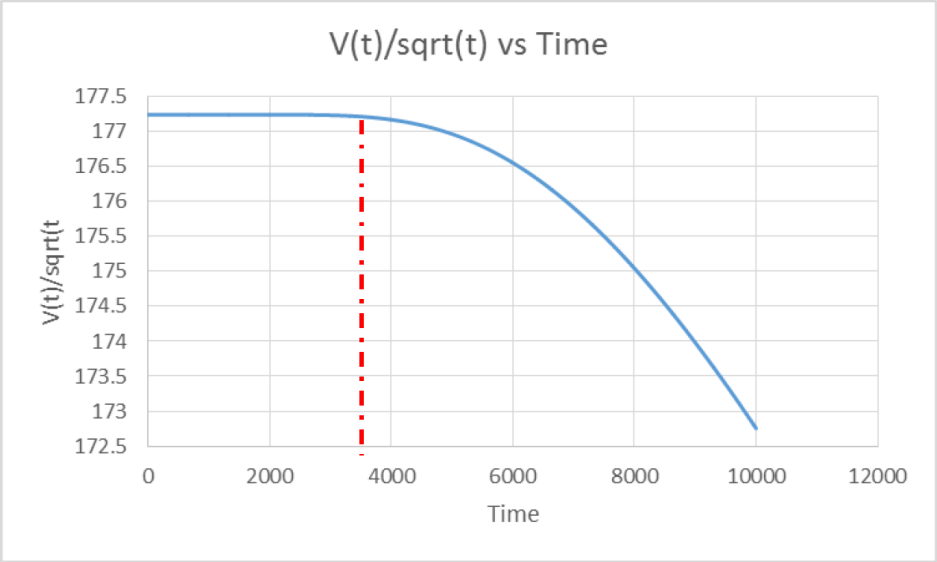

Figure 28: Plot of Analytical V(t)/$\sqrt{t}$ vs Time

Instead of computing drainage volume for the entire sample, we will only calculate the drainage volume ((Vf(t)) for the nodes on the plane opposite to seed node plane and divide it by square root of time using the Equation (2.41) for a planar seed node simulation. The purpose of just using the drainage volume of the opposite plane nodes is to identify more easily the time when the pressure transient has reached the opposite end. The time value can be easily located in Figure 29 denoted by the red line.

$$\frac{Vf(t)}{\sqrt{t}} = \frac{\sum PV_j * e^{-\frac{\tau_j^2}{4t}}}{\sqrt{t}} \tag{2.41}$$

In Equation (2.41), PV_j is the volume of the nodes on the plane opposite to the seed node plane and τ_j is the DTOF value for the nodes on the plane opposite to the seed node plane.

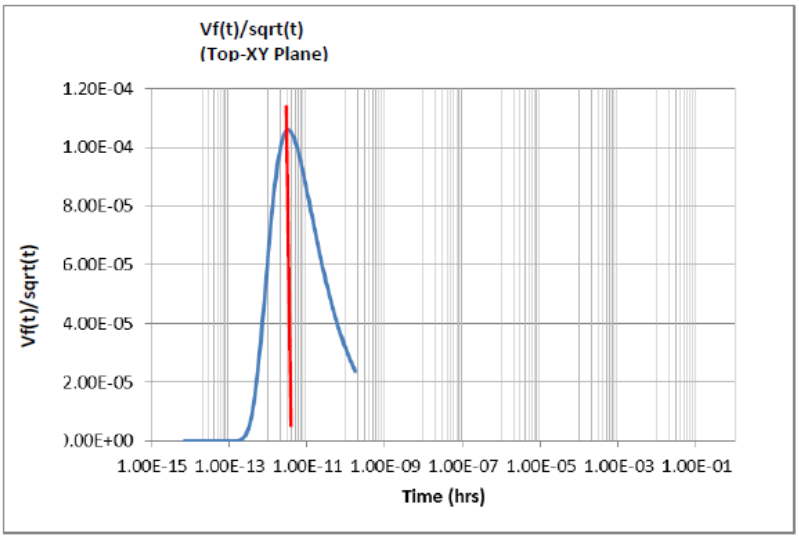

Figure 29: Vf(t)/$\sqrt{t}$ vs Time on the Top XY Plane for Bottom XY Plane Seed Nodes

In Figure 29, Vf(t)/$\sqrt{t}$ will increases up to a certain time up to which the pressure disturbance reaches the opposite plane. Thereafter, it starts to decrease since the volume of the nodes on the opposite plane have been drained completely thereby leading to the decrease in the value of Vf(t)/$\sqrt{t}$.

$$k = \frac{\phi \mu c_t * {r_{inv,linear}}^2}{2t} \tag{2.42}$$

The DOI ($r_{inv,linear}$) in Equation (2.43) is the distance between the two opposite planes. The time (t) in Equation (2.42) is the time at which the Vf(t)/$\sqrt{t}$ reaches its maximum value. Now, we can calculate the value of permeability (k) from Equation (2.42) since we know the value of the other parameters (Table 6).

Parameter	Value
Viscosity (μ)	0.2 cp
Porosity (ϕ)	0.28 (carbonate), 0.26 (synthetic sandstone)
Compressibility (c_t)	3e-05 psi-1
DOI ($r_{inv,linear}$)	$5 * 2\sqrt{2} * R_{grain} = 0.00289$ (ft) (Synthetic Sandstone) Δx=0.024 ft., Δy=0.021 ft., Δz=0.027 ft. (Carbonate)

Table 6: Parameter Values used for DOI Analysis. *The values in the table should be used with appropriate conversion factors.*

The permeability calculated using DOI analysis is a planar permeability while the permeability calculated using the derivative analysis is a line permeability. We have to convert the planar permeability to line permeability for the carbonate pore network because of different values of permeability in different directions. The synthetic sandstone doesn't need such conversion because it doesn't have any directional anisotropy since it has been randomly generated.

$$q_{line} = W_i(P_{cell} - P_{wf}) \tag{2.43}$$

$$W_i = \frac{2\pi\sqrt{k_x k_y}h}{\log(\frac{r_w}{r_o})} \tag{2.44}$$

Equation (2.43) and Equation (2.44) (Peaceman, 1983) give the rate (q_{line}) for a line source in the Z-direction in standard units. The equivalent permeability is the geometric mean of the X direction (k_x)and Y (k_y) direction planar permeability values. Similarly, the equivalent permeability for Line-X would be the geometric mean of the Y and Z direction planar permeability values and so on.

3. VALIDATION ON SYNTHETIC SANDSTONE MODEL

3.1 Synthetic Pore Network Description

A synthetic pore lattice network was developed to mimic a natural sandstone pore network. Sandstone pore networks occurring naturally are single porosity in nature. The bond radius of the sandstone pore networks are smoothly varying distributions with some order of variance in the bond radius (Figure 30).

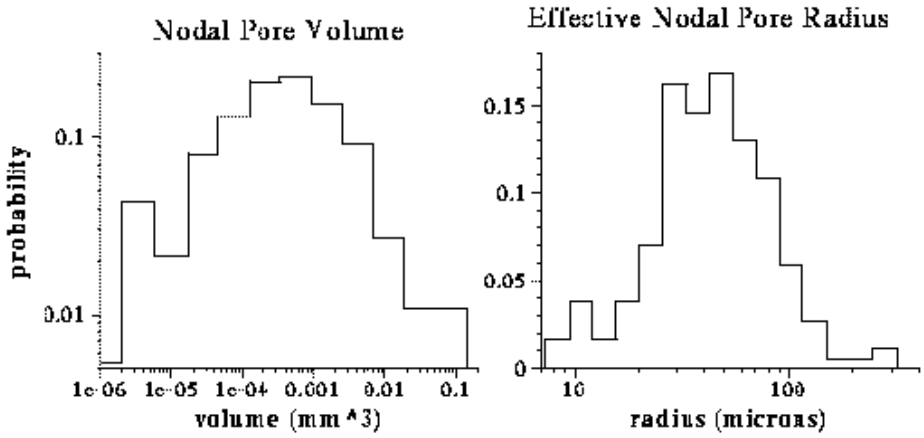

Figure 30: Bond Radius and Pore Volume Distribution of Naturally Occurring Fontainebleau Sandstone (Lindquist et al. 1999)

Another characteristic of sandstones is that they have porosities in the range of 5%-30% (Courtesy Argonne National Laboratory website) usually. Therefore our synthetic model should incorporate these basic characteristics of the sandstone pore structure i.e. smoothly varying distribution of bond radius and porosity in the range of 5%-30%.

3.1.1 Rationale for the Synthetic Model

The process of formation of sandstone involves the aggregation of sand grains and then compaction under pressure for millions of years. Therefore we have considered the tightest packing of spherical grains that is possible in a homogeneous geometry. We don't account for the deformation and cementation since it would be too complex to model and also because of the fact that the homogeneous geometry model gives a porosity of 26% which is within the naturally occurring sandstone porosity range. Kepler's conjecture states that the tightest packing of equal radii spheres possible would have a porosity of 26%. This porosity is within the range of porosities found in sandstone rocks.

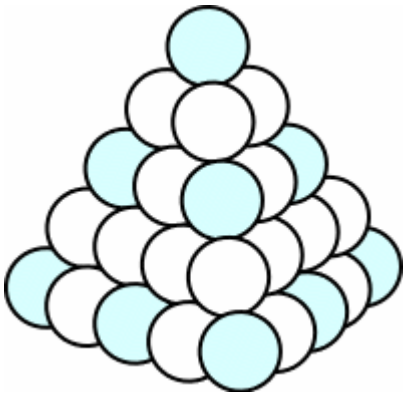

Figure 31: Kepler's Conjecture Representation (Hales, 2001)

The Figure 31 shows a demonstration of Kepler's conjecture. It is an arrangement of equal radii spherical balls in 2 alternating layers. This structure has a

packing density of 74% and it is also commonly known as the Hexagonal Close Packing (HCP) geometry.

3.1.2 Model Construction Technique

For our synthetic model we are working with the Face Centered Cubic (FCC) model. This model also satisfies Kepler's conjecture which means it has a porosity of 26%.

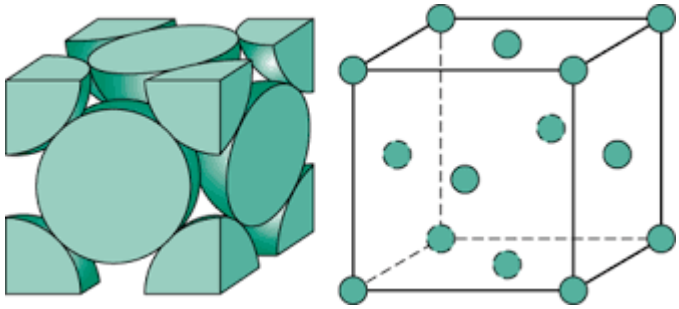

Figure 32: Face Centered Cubic (FCC) Model (Eliasson, 2015)

Figure 32 shows a representation of the FCC model. The model has ½ sphere present on each face of the cube and $1/8^{th}$ sphere present on each corner of the cube. This means that a total of 4 spheres are present in one unit cell of the model. The spheres in the unit cell are the sand grains for our purpose.

There exist void spaces in between the sand grains which can be seen in the above figure also. These void spaces will hold the fluid and provide a pathway for the fluid to flow. These void spaces will be the bonds in our pore network model whose radii will be varied to generate the unimodal bond radius distribution seen in sandstones. But

first we need to understand the geometry of these void spaces so that they can be accurately modeled as bonds in our network model.

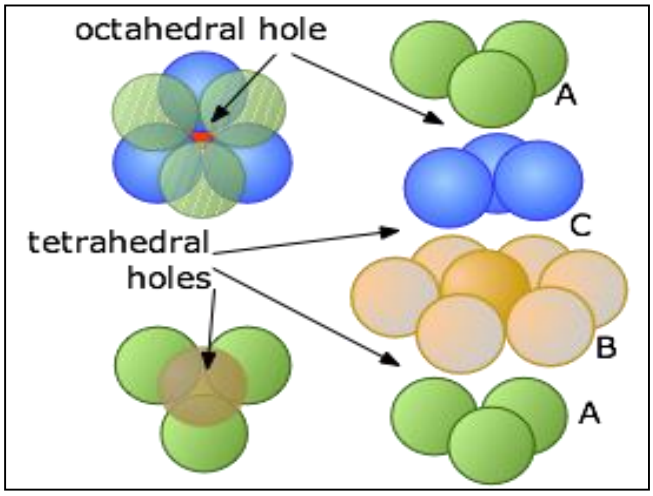

Figure 33: Octahedral and Tetrahedral Void (Courtesy UC Davis)

There are two types of void spaces present in the FCC model. These are octahedral and tetrahedral voids. A tetrahedral void is derived from the fact that it is the empty space formed by placing the centers of four spheres at the four corners of a regular tetrahedron (Figure 33). The octahedral void is the empty space at the center of the structure formed by placing one tetrahedron on top of another tetrahedron upside down and rotated by 60 degrees (Figure 33).

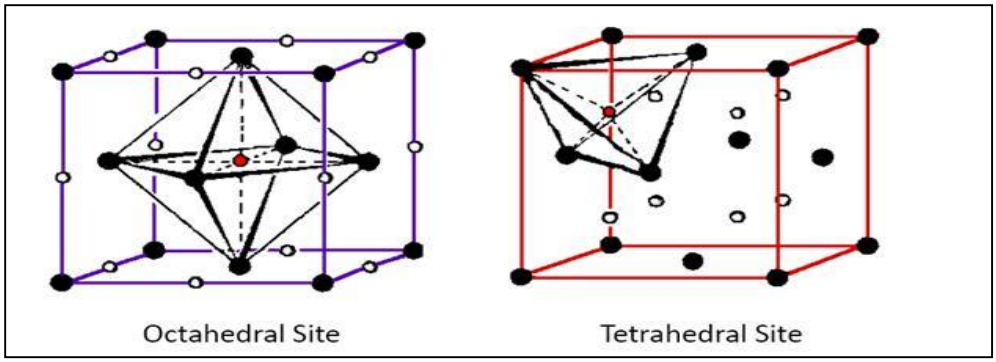

Figure 34: Void Spaces in the FCC Model (Courtesy University of Kiel)

Figure 34 shows the location of the void spaces in the FCC model. The right figure in Figure 34 shows the location of tetrahedral voids as white circles. There are eight tetrahedral voids in the model i.e. one for each corner. The tetrahedral void is located along the body diagonal at a distance of $1/3^{rd}$ the length of the body diagonal from the vertex of the unit cell. The octahedral voids are located at the center of each each edge and at the center of the model as shown by the white and red circles in the left figure of Figure 34 respectively. The octahedral void located on the edge is $1/4^{th}$ the size of a complete octahedral void and the one at the center is a complete octahedral void.

Number of Nodes	
Tetrahedral Node	Octahedral Node
8 full nodes	12 quarter nodes for each edge and 1 full node at the center of the unit cell
Volume of Nodes (m^3)	
Tetrahedral Node	Octahedral Node
$0.1708R_{grain}^3$	$1.4652R_{grain}^3$
Length of Bonds (m)	
Tetrahedral to Octahedral	Edge Octahedral to Central Octahedral
$0.5857R_{grain}$	$1.172R_{grain}$
Coordination Number	
Tetrahedral Node	Octahedral Node
4	20

Table 7: List of Void Spaces and their Volumes in the FCC Model

The radius of the grain (R_{grain}) was assumed to be 0.0625 mm or 0.000205 ft. (Grain Size scale, Univ. of Rochester website). This is in the range of the fine grained sandstone. There are some correlations for getting an estimate of steady state permeability values in a random packing of equal spheres. One of them is the Carman-Kozeny (Kaviany, 2012) model described in Equation (3.1).

$$k = \frac{\phi^3}{36l(1-\phi)^2} D_{grain}^2 \tag{3.1}$$

The Equation (3.1) is in standard units where l=5 and D_{grain} is the diameter of the grain. For our grain radius of 0.0625 mm, the model predicts a permeability value of 2900 md. Our actual steady state permeability is 6700 md. The permeability value from steady state simulation is in the same order of magnitude but higher than the Carman-Kozeny model permeability. The steady state calculation will be the reference for our

analysis in the future. The calculation using the Carman-Kozeny model was just to show that our model is a realistic representation.

The coordination number is the average number of nodes attached to each node. The nodes in the model will represent the volume that is contained in the void spaces. The bonds in the model will represent the distances between the centers of the void spaces in the FCC model. The calculation of the length of these bonds is shown in Appendix B. The bonds occur between the tetrahedral nodes and the octahedral nodes as well as between the edge octahedral nodes and the central octahedral nodes in a particular unit cell.

The next thing which we determined is the radius of the bonds in the pore network. The radius of the bond is decided by the fact that the fluid flowing in and out of these void spaces will encounter maximum resistance at the narrowest parts of these voids. This void space can be visualized as the projection of the empty space in between three equal spheres lying on a plane on 2-dimensions.

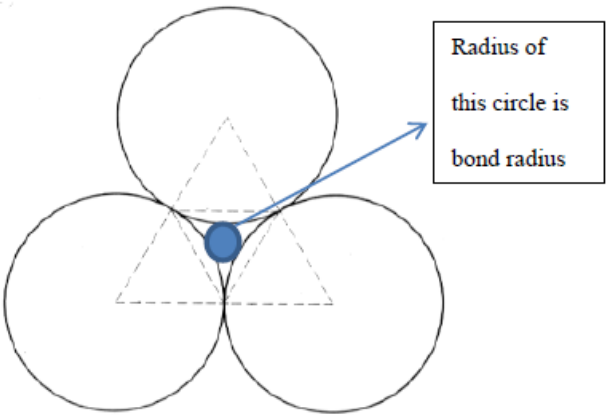

Figure 35: Radius of Bond in Synthetic Pore Network

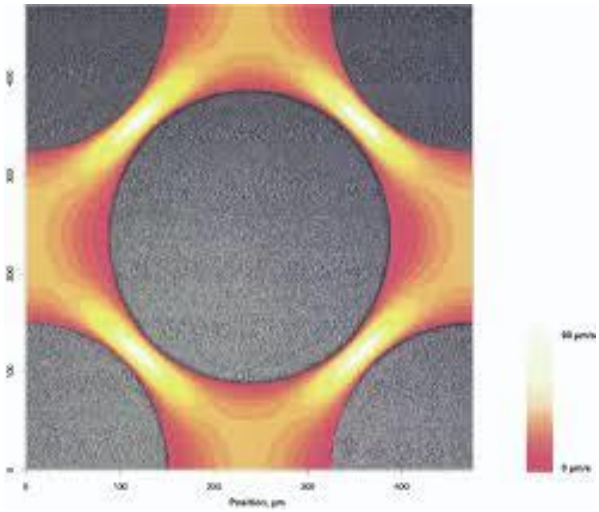

Figure 36: Velocity Profile between Grains. The Grey Areas Represent the Grains. The Progression from Red to Yellow Denotes Increasing Velocity (Baumann et al. 2004)

Figure 36 shows that the velocity is maximum for the parts which is farthest away from the grain walls. The velocity is almost zero at the grain walls. Therefore, the velocity in between grains will be highest in the central circular portion as shown in

Figure 35. The radius of this central circular section will act as the bond radius having a value of $0.1547R_{grain}$.

$$k_{bond} = \frac{{R_{bond}}^2}{8} \tag{3.2}$$

$$\tau_{bond} = \sqrt{\frac{\phi \mu c_t}{k_{bond}}} * L_{bond} \tag{3.3}$$

Equation (3.2) is used to calculate the permeability of the bonds. Equation (3.3) is used to calculate the DTOF value of the bonds where L_{bond} is the length of the bond.

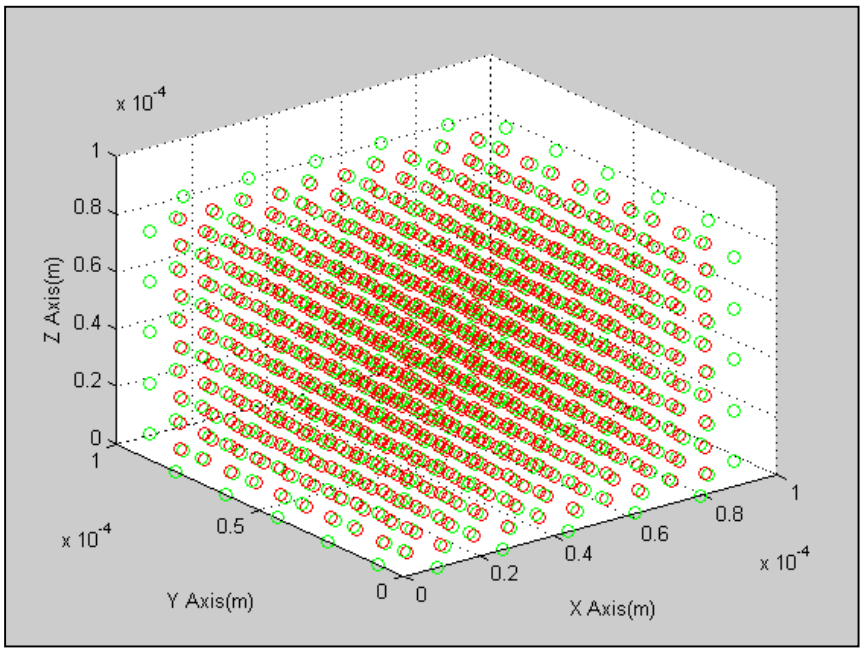

Figure 37: Visualization of All the Nodes in the Synthetic Sandstone Pore Network. The Red Circles Denote the Tetrahedral Nodes and the Green Circles Denote the Octahedral Nodes. There are a Total of 2625 Nodes in the Synthetic Sandstone Pore Network.

The unit cell is arranged in a 5x5x5 arrangement in three dimensional space (Figure 37). The unit cell connects to another unit cell on all its faces. The bonds connecting the unit cell are between the octahedral nodes. The lengths of these connecting bonds are zero because in essence the octahedral nodes/voids in adjacent unit cells are one single octahedral void space. Therefore, if a pressure wave reaches one part of this octahedral void/node in a unit cell, in effect it reaches all the adjoining octahedral nodes/voids in the adjacent unit cells.

To make our model more realistic is to introduce heterogeneity in the model. We do so by varying the bond radius in the model. The bond radius directly affects the permeability value which in turn affects the DTOF value of the bonds. The bond radius is sampled randomly from a normal distribution of mean radius as the calculated bond radius and variance as a percentage of the mean. The variance of these normal distributions can be varied to increase or decrease the amount of heterogeneity introduced in the model.

Type of Model	**Standard Deviation for Bond Radius Distribution**
Homogeneous	0
Slightly Heterogeneous	0.2
Highly Heterogeneous	0.9

Table 8: Standard Deviation Values for Bond Radius Distribution in Synthetic Sandstone Pore Network

Three different values of variance have been used on our model to introduce different amounts of heterogeneity in the model (Table 8).The heterogeneity was introduced by keeping the bond radius of the octahedral and tetrahedral bonds different and randomly sampling from distributions with different values of standard deviation. Bond radius is varied by randomly picking radius values from a distribution with a mean value of $0.1547 * R_{grain}$and $0.1547 * R_{grain}/2$ for the octahedral-octahedral node bond and the octahedral-tetrahedral node bond respectively.

Type of Model	**Maximum Bond Permeability (md)**	**Minimum Bond Permeability (md)**	**Mean Bond Permeability (md)**
Homogeneous	11600	11600	11600
Moderately Heterogeneous	12605	0.2404	3126
Highly Heterogeneous	204310	8.4303e-06	8288

Table 9: Bond Permeability Ranges in the Synthetic Pore Network

3.2 Results

The synthetic model described previously was used to test our algorithms using the derivative analysis method and the analytical derivative method. The results from both the methods are presented in the following sections. The results show good agreement with the expected permeability values.

3.2.1 Analysis using the Well Test Derivative Method

The seed nodes can be aligned in X, Y or Z direction. Since our model is cubical in shape and the heterogeneities introduced are random in nature, all the available directions of seed nodes would give almost identical results. For analyzing the synthetic model we have assumed a seed node direction along a Z-line (Figure 38).

The seed nodes act as a line source at the center of the sample. The pressure wave spreads out from the seed nodes and reaches the boundaries of the sample. Therefore, this kind of a system can be analyzed by using conventional line source solutions.

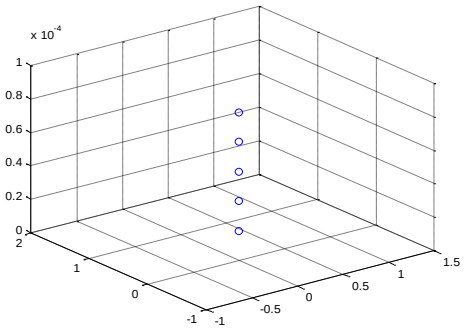

Figure 38: Seed Node Configuration (Line-Z)

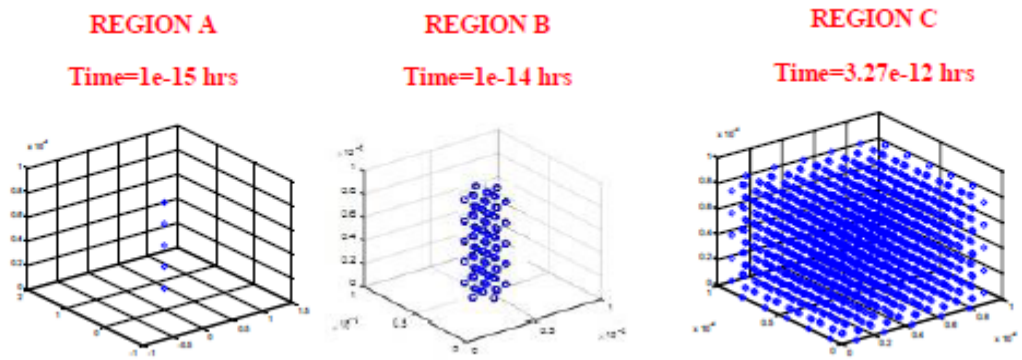

Figure 39: Visualization of Drainage Volume vs Time for Homogeneous Synthetic Pore Network (the Nodes are Getting Drained Equally on All Sides)

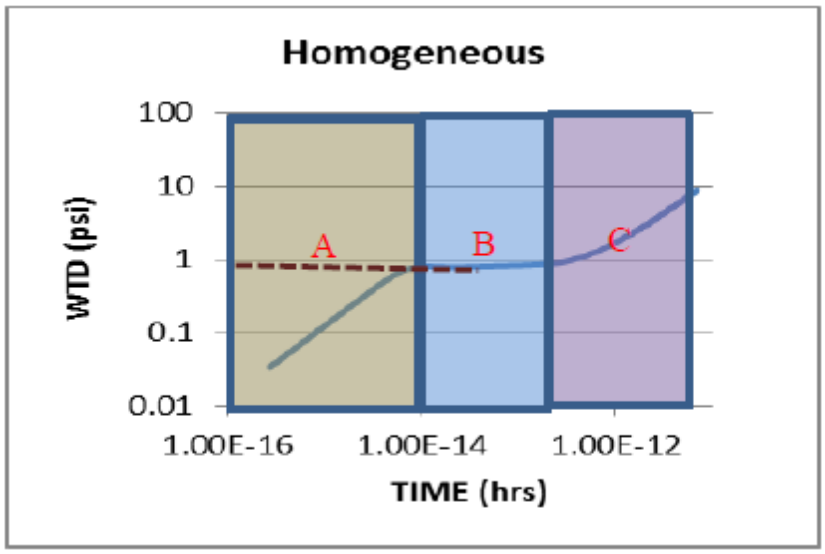

Figure 40: Visual Comparison of Well Test Derivative and Drainage Volume for Homogeneous Synthetic Sandstone Pore Network

Next, we will analyze the drainage volume evolution and compare the changes in the well test derivative for the homogeneous synthetic sandstone pore network. The Equation (2.16) gives the method to obtain the simulated well test derivative at different

times of simulation. In the well test derivative plot (Figure 40), we can see that the derivative increases initially over a very small time (Region-A in Figure 40). This is because only the neighboring nodes to the seed nodes are getting drained (Figure 39) at this time which is resulting in an almost constant drainage volume ($V(t)$) while the time is increasing. This is the equivalent of wellbore storage in which PSS occurs at the wellbore. Next, we notice an almost constant well test derivative (Region-B in Figure 40) interpreted as the IARF (Infinite Acting Radial Flow) flow regime for the network model. At this stage, both time and the drainage volume (Figure 39) are increasing in such a way that the well test derivative (Equation (2.16)) remains constant. Finally, we can see that the well test derivative is increasing (Region-C in Figure 40). This can interpreted as a PSS (pseudo steady state). The drainage volume has covered the entire model (Figure 39) and has become constant. Therefore, the well test derivative is increasing linearly with time (Refer Equation (2.16)).The IARF region in the well test derivative can be analyzed to estimate the permeability of the synthetic pore network by using Equation (2.21) and Equation (2.22).

Now we will analyze the drainage volume patterns in a heterogeneous synthetic pore network (Figure 41). The early time drainage volume for the synthetic model shows nodes being drained at distances far from the seed nodes. The middle time drainage volume also shows the irregular drainage pattern. These drainage patterns show that our algorithms are effective for all kinds of heterogeneity.

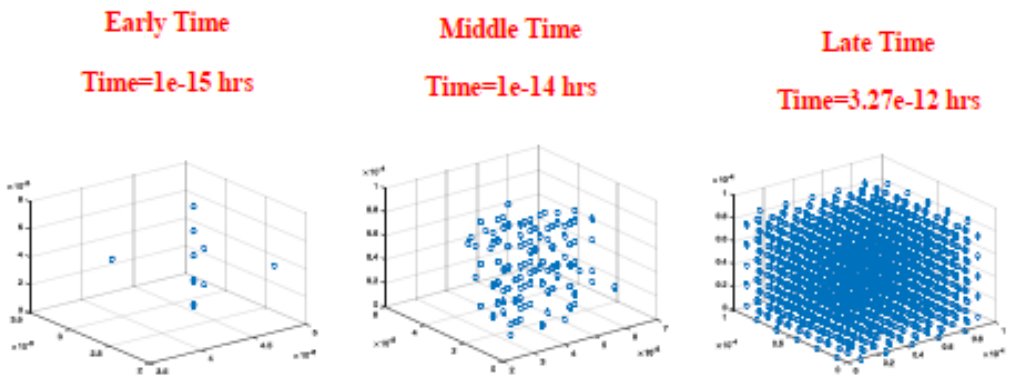

Figure 41: Visualization of Drainage Volume for the Highly Heterogeneous Synthetic Pore Network

Now we are going to study well test derivative analysis results for the synthetic pore network (Figure 42). The network was tested for various amounts of heterogeneity. We can see that the IARF period in the moderately heterogeneous period was shortened in comparison to the completely homogeneous case. This is due to the presence of some high permeability bonds which are causing a small linear transitional flow before the IARF starts. The IARF period in the highly heterogeneous plot is even more shortened due to the presence of more high permeability bonds.

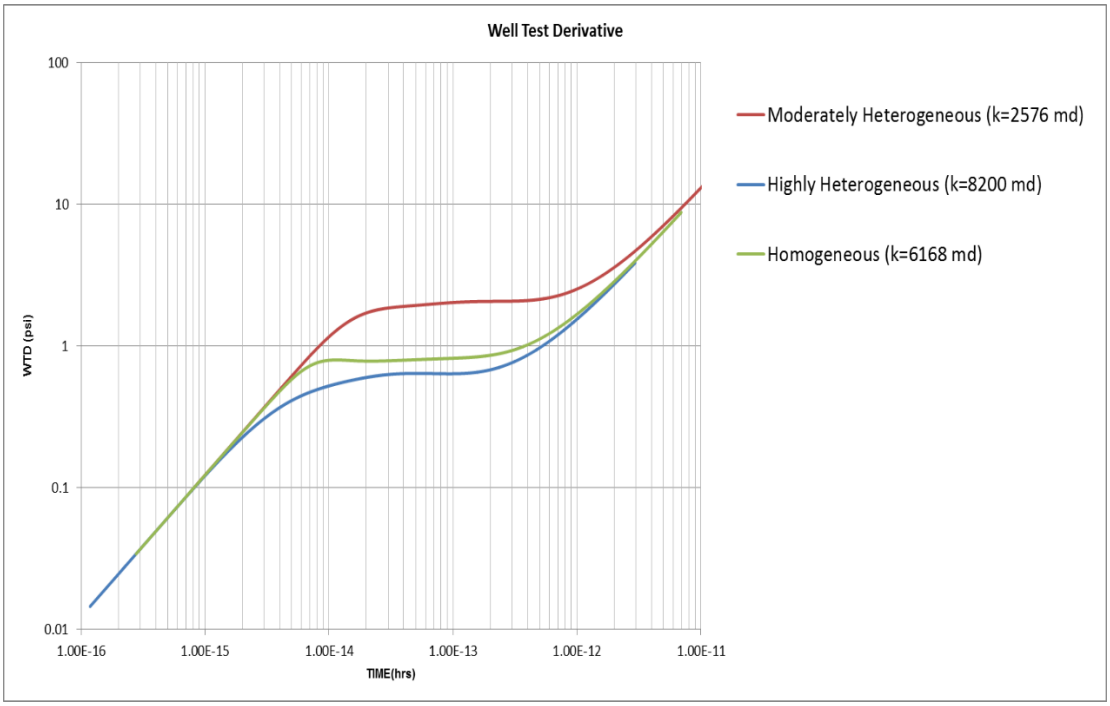

Figure 42: Comparison of the Simulated Well Test Derivative Plots for Line Z Seed Node Simulation among Different Degree of Heterogeneity Synthetic Pore Network Models

Here, we present the results from the well test derivative analysis and compare them with the mean bond permeability of the synthetic pore network. The well test derivative permeability values are within the range of the bond permeability values. The mean bond permeability values are within 50% of the well test derivative permeability values. The homogeneous WTD permeability is about half the mean bond permeability. This can be attributed to the tortuosity present in the pore network since higher tortuosity leads to lower permeability (Ahmad et al. 2005).

Type of Model	Minimum Bond Permeability (md)	Maximum Bond Permeability (md)	Mean Bond Permeability (md)	Well Test Derivative permeability (md)
Homogeneous	11600	11600	11600	6168
Moderately Heterogeneous	0.2904	12605	3126	2576
Highly Heterogeneous	8.403e-06	204310	8288	8200

Table 10: Synthetic Model Permeability Results from the Analysis of the Well Test Derivative

3.2.2 Analysis using the Depth of Investigation Method

The DOI (Depth of Investigation) concept is used to get an estimate of the permeability in this method. A particular plane acts as seed nodes for the simulation to start (Figure 43). The wave front will follow the path of least DTOF to the opposite plane. If the pore network is homogeneous, then the DTOF value for all the paths will be the same. If the pore network is heterogeneous, the wave front will reach the opposite plane fastest by taking the path with the least DTOF.

The time at which the quantity Vf(t)/$\sqrt{t}$ reaches maximum for the plane opposite to the seed node plane is the time at which the DOI is equal to the distance between the planes. This concept has been explained in detail earlier in Section 2.4.

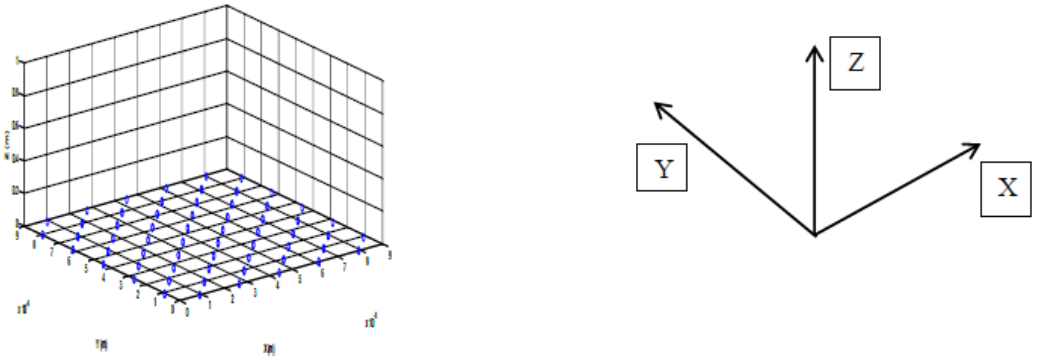

Figure 43: Seed Node Configuration for Synthetic Sandstone Pore Network (Bottom Plane XY)

The plots of Vf(t)/$\sqrt{t}$ on the plane opposite to seed node plane vs time are shown below. The analysis method for getting permeability value from these plots has been discussed before. The distance between planes was calculated as $5 * 2\sqrt{2} * R_{grain}$.

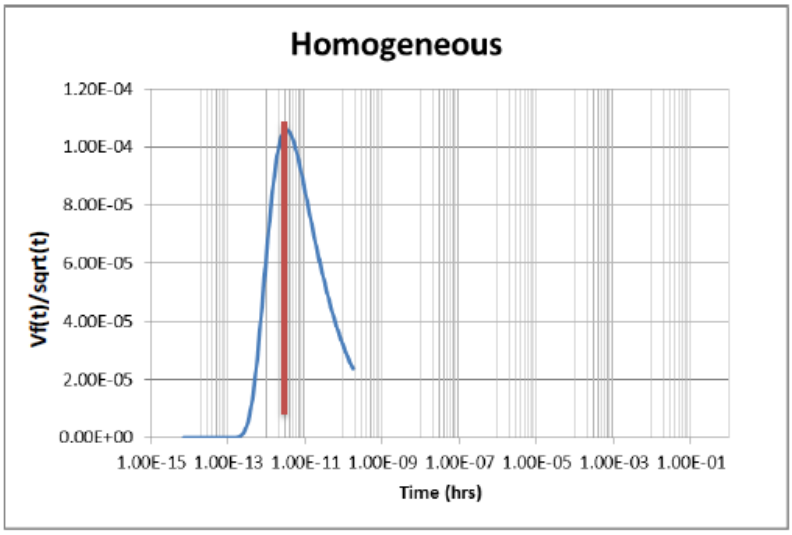

Figure 44: Vf(t)/$\sqrt{t}$ (Top XY Plane) vs Time for Bottom XY Seed Nodes for Homogeneous Network

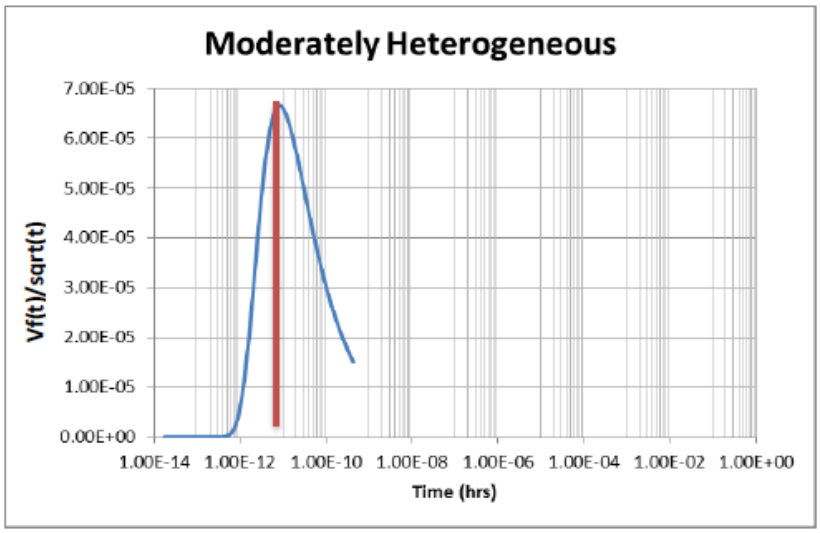

Figure 45: Vf(t)/$\sqrt{t}$ (Top XY Plane) vs Time for Bottom XY Seed Nodes for Moderately Heterogeneous Network

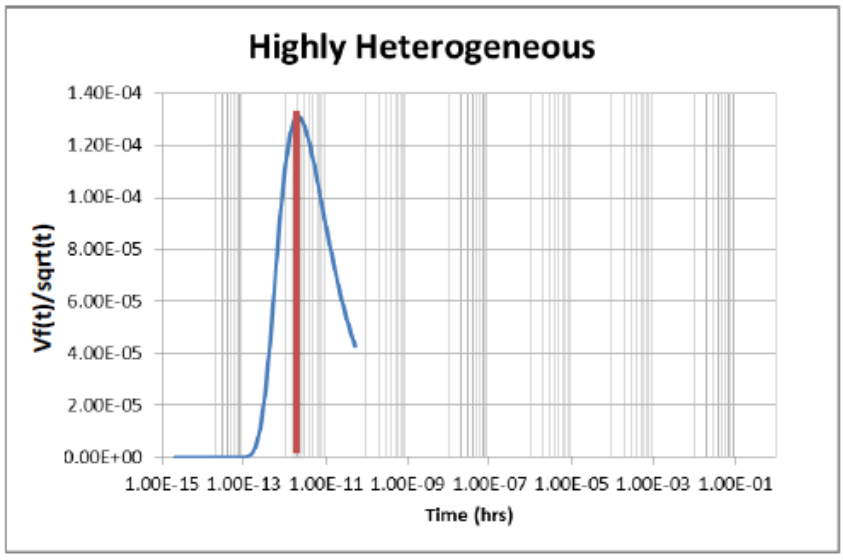

Figure 46: Vf(t)/$\sqrt{t}$ (Top XY Plane) vs Time For Bottom XY Seed Nodes for Highly Heterogeneous Network

Model	Average Permeability Range of Bonds in the network (md)	DOI (m)	Time at maximum Vf(t)/$\sqrt{t}$ (hrs)	Permeability (md)
Homogeneous	11600	0.0000883	3.194e-12	8800
Moderately Heterogeneous	3126	0.0000883	8.396e-12	3100
Highly Heterogeneous	8288	0.0000883	2.02e-12	12300

Table 11: Permeability Values Obtained from DOI Analysis of Synthetic Sandstone Pore Network

Table 11 shows that permeability values obtained from the DOI analysis are within 40 % of the mean permeability of the bonds in the synthetic sandstone pore network.

A steady state analysis was done for the synthetic sandstone pore network. The comparison of all analysis methods is shown in Table 12. The analysis shows that the derivative analysis method gives estimated permeability values to within 50% of the mean permeability of bonds. The DOI method is capturing the effect of lowest DTOF path or the paths with the highest permeability. As the heterogeneity of the model increases, there are more high permeability paths present due to which the DOI method gives higher permeability values. The DOI method is giving permeability estimates which are within 30 % of the mean permeability values for the low heterogeneity cases and within 60 % of the mean permeability for the high heterogeneity case.

The transient techniques more precisely capture the effects of the initial passage of a pressure wave. This initial passage is through the well-connected high permeability sub-section of the pore network. The steady state technique captures the effect of long time behaviour when the pressure wave has reached all parts of the pore network. As the heterogeneity of the pore network increases, the number and connectivity of well-connected high permeability sub sections also increases. This would lead to an increase in the ratio of the permeability value being captured by transient technique to the permeability value from the steady state technique. This increasing ratio can be observed in the results in Table 12.

Model Type	Homogeneous	Moderately Heterogeneous	Highly Heterogeneous
Minimum Bond Permeability (md)	11600	0.2904	8.403e-06
Maximum Bond Permeability (md)	11600	12605	204310
Average Permeability of Bonds in the network (md)	11600	3126	8288
k(md) (Steady State Analysis)	6700	1320	7540
k(md) (Well test Derivative Analysis)	6168	2576	8200
k(md) (DOI Analysis)	8800	3100	12300

Table 12: Comparison of Results for the Synthetic Pore Network among the Well Test Derivative Analysis, DOI Analysis and Steady State Analysis Methods

4. APPLICATION ON CARBONATE PORE NETWORK

4.1 Carbonate Pore Network Description

The carbonate pore network used for our analysis was extracted from a micro-CT scan of a carbonate core of dimensions (12.4 mm dia. and 14.1 mm length). The micro-CT scan was analyzed and the pore network was extracted by using AVIZO software (Pasumarti, 2014).

4.1.1 Pore Network Generation

A small rectangular cuboid section (7.5 mm x 6.5 mm x 8.5mm) of the original sample micro-CT scan image (Figure 47) located towards the center of the original sample was used for constructing the network model to remove any imaging artifacts.

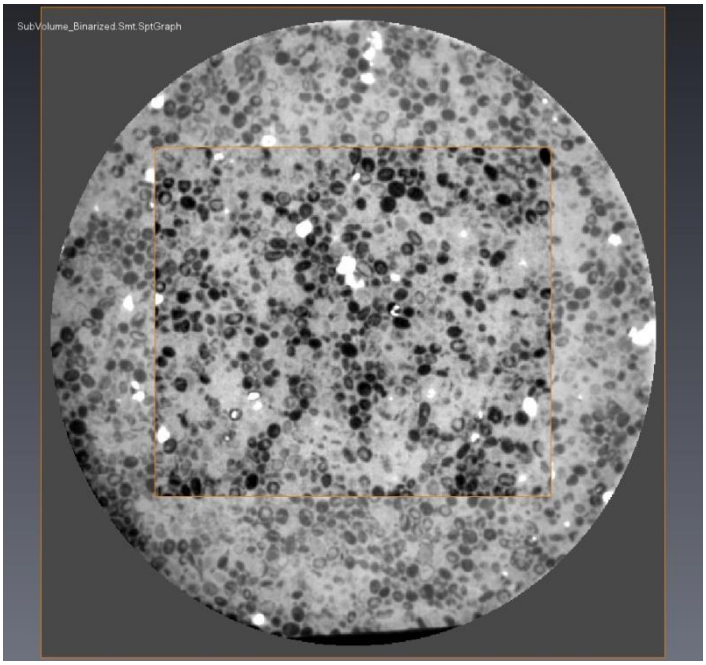

Figure 47: Micro CT Scan Image of the Sample (Pasumarti, 2014)

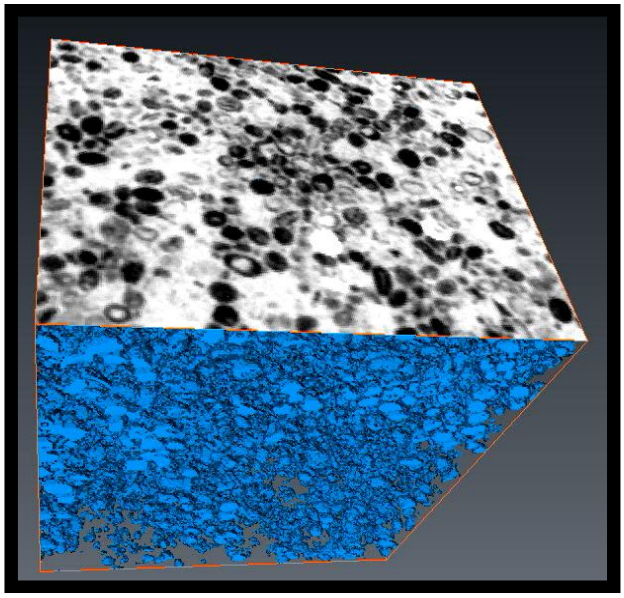

Figure 48: Binarization of the Carbonate Micro-CT Scan Image Using AVIZO (Pasumarti, 2014)

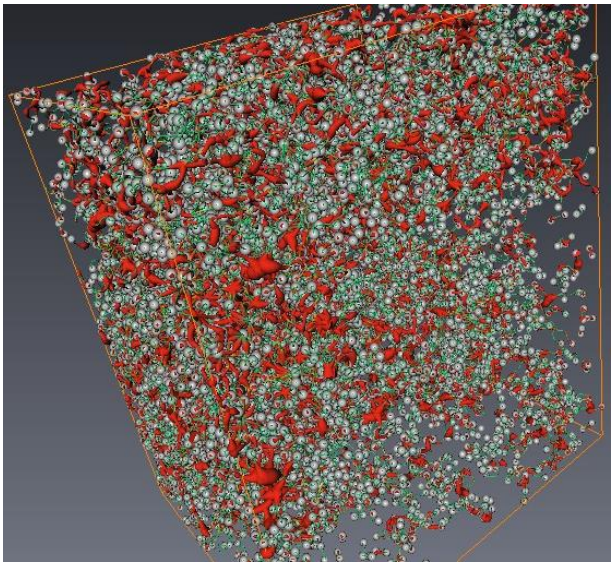

Figure 49: Pore Network Obtained from Micro-CT Scan of the Carbonate (Pasumarti, 2014)

The binarization process (Figure 48) was determined using AVIZO software (Pasumarti, 2014). This process extracts the pore space from all the micro-CT scans and designates the other space as non-porous space. After binarization, the AVIZO software was used to construct the pore network model (Figure 49). After the construction, the software gives a list of nodes, their location in space, list of bonds, length and radius of the bonds and the connection list of bonds and nodes.

The bond radius is available from which a permeability value for each bond is calculated using the analogy of Poiseuille flow.

$$k_{bond} = \frac{{R_{bond}}^2}{8} \qquad q_{poiseuille} = \frac{\pi R_{bond}^4 \Delta p_{bond}}{8\mu L_{bond}} \tag{4.1}$$

Once the permeability of the bond is known, the DTOF for each bond is calculated using the following relationship.

$$\tau_{bond} = \sqrt{\frac{\phi \mu c_t}{k_{bond}}} * L_{bond} \tag{4.2}$$

Finally we have a value of DTOF for all the bonds in the network, volume of all the nodes in the network and a list of connections among the bonds and nodes. A particular set of seed nodes are chosen and the simulation was performed using the Dijkstra algorithm described previously.

4.1.2 Pore Network Statistics

The carbonate pore network extracted is from an outcrop field sample. The figure below shows the distribution of throat sizes in the network model. It can be seen that it is a bimodal distribution of pore throats (Figure 50). There are a large number of throats (bonds) which have a small throat radius around 10 μm and a small number of throats

which have a large throat radius around 300 µm. The bonds having the smaller throat radius can be interpreted as the intra-granular pores which hold the majority of the fluids. The smaller percentage of bonds having larger bond radius can be interpreted as the intergranular pore space which provide the pathway for the fluid to flow through the carbonate.

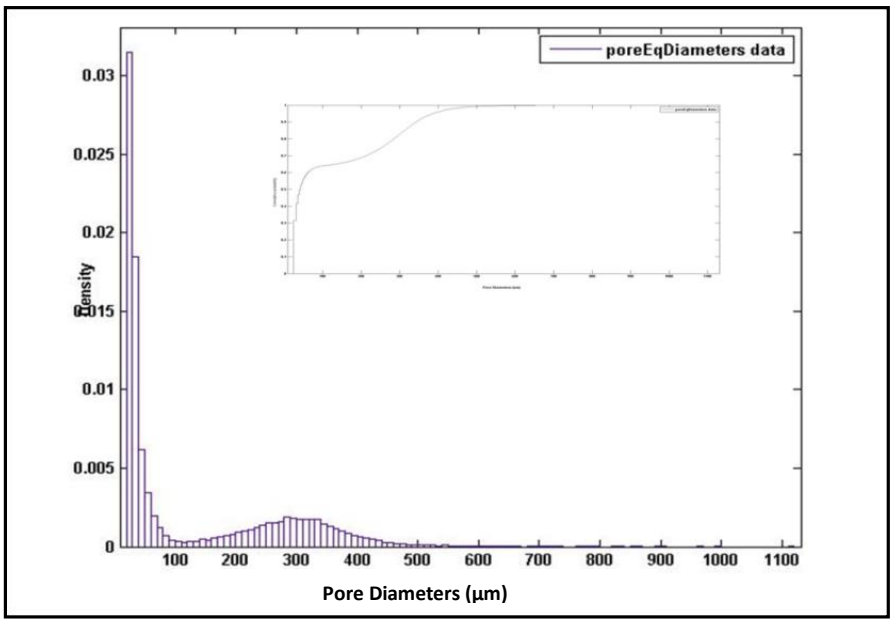

Figure 50: Pore Throat Size Distribution (Pasumarti, 2014)

4.2 Results

The carbonate pore network was analyzed using the well test derivative and DOI analysis methods explained previously. The results of the analysis are presented in the following sections.

4.2.1 Analysis using the Well Test Derivative Method

A particular set of seed nodes along the direction of X, Y or Z along the center of the sample is used to start the simulation. This acts as the line source for the sample. The line source solutions for dual porosity are well known and have been discussed previously. The following three figures are used to visually analyze a Line-Z seed node simulation in the carbonate pore network (Pasumarti, 2014).

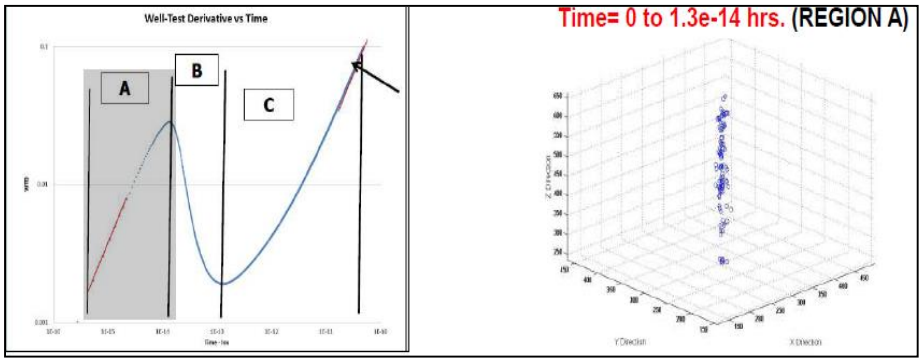

Figure 51: The Left Figure Shows the Well Test Derivative Curve and the Right Figure Shows the Drainage Volume Visualization for the Shaded Region in the Derivative Plot (Pasumarti, 2014)

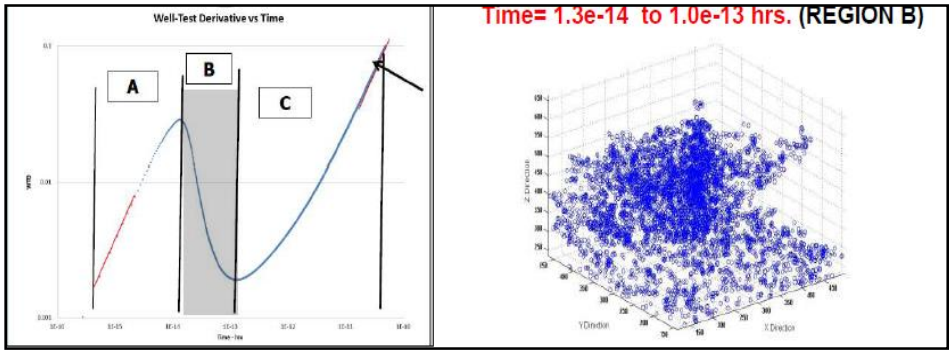

Figure 52: The Left Figure Shows the Well Test Derivative Curve and the Right Figure Shows the Drainage Volume Visualization for the Shaded Region in the Derivative Plot (Pasumarti, 2014)

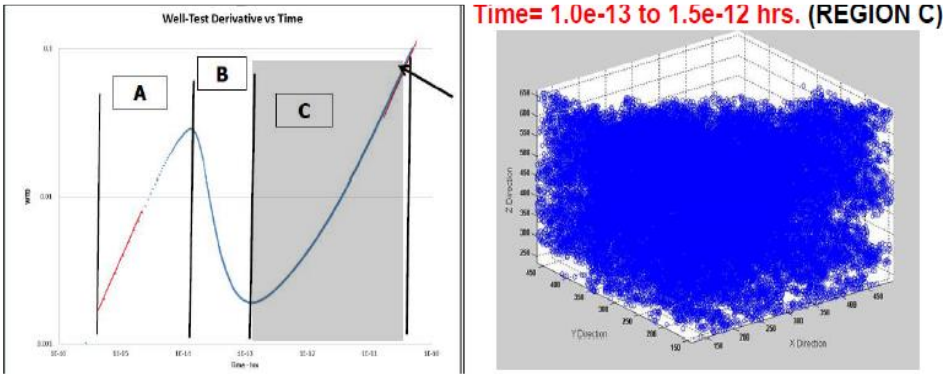

Figure 53: The Left Figure Shows the Well Test Derivative Curve and the Right Figure Shows the Drainage Volume Visualization for the Shaded Region in the Derivative Plot (Pasumarti, 2014)

The simulated well test derivative (Equation (2.16)) increases at very small time due to the almost constant drainage volume (Region-A). At this time, only the well-connected inter-granular pores are draining. Then there is a sudden decrease in the derivative value (Region-B). During this decrease, it can be seen that that the drainage volume (V(t)) increases at a very large rate with respect to time. This causes the decrease in the well test derivative (Equation (2.16)). During this time, the poorly connected but large volume intra-granular pores are draining into the intergranular pore spaces. Then, the well test derivative starts to rise slowly as the rate of increase in drainage volume starts to decrease and the drainage volume finally becomes constant (Region-C). This is the time when PSS is reached and it can be seen on the well test derivative plot as a unit slope line.

Next, we study the results for the well test derivative analysis to compute permeability and other transport parameters in the carbonate pore network sample. The Figure 54 shows the method of getting storativity ratio value from the well test

derivative plot. This process has been described in detail in Section-2.3. Figure 55 shows the fitting of the simulated well test derivative with analytical well test derivative by varying the parameters (k_{fb}, λ, ω) for Line-Z.

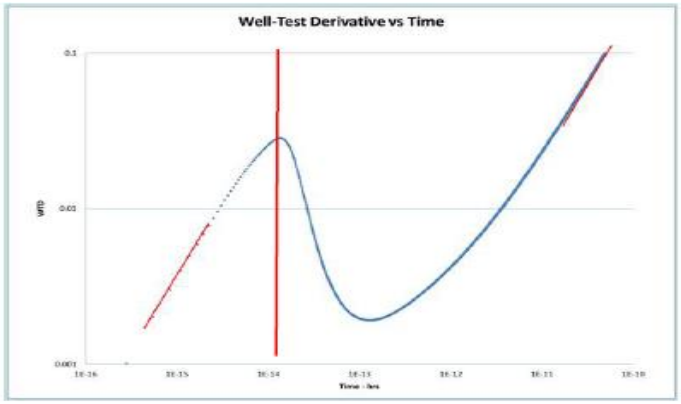

Figure 54: ω Determination for Line-Z Seed Nodes for Carbonate Pore Network (Pasumarti, 2014)

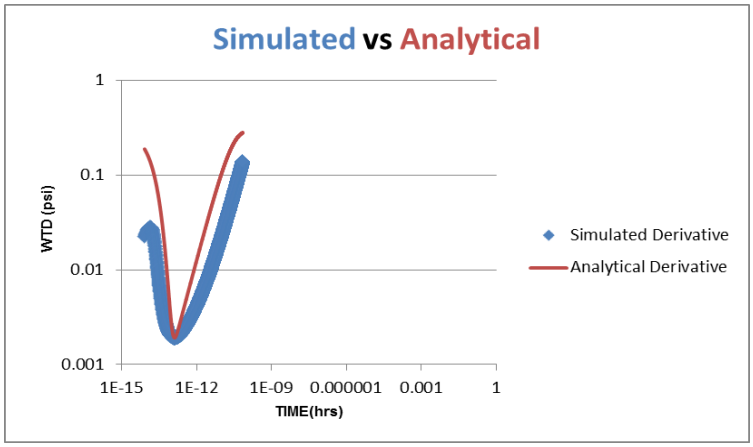

Figure 55: Match of the Simulated and Analytical Well Test Derivative for Line-Z Seed Nodes for Carbonate Pore Network

Figure 56 and Figure 57 show the fitting of the simulated well test derivative with analytical well test derivative by varying the parameters $(k_{fb}, \lambda, \omega)$ for Line-X and Line-Y respectively.

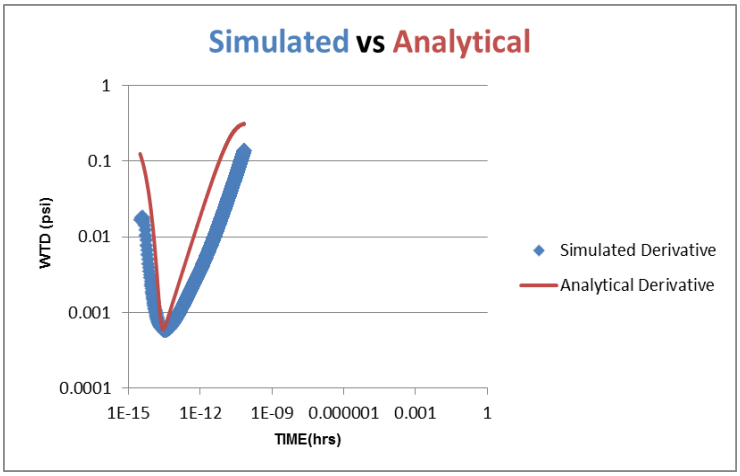

Figure 56: Match of the Simulated and Analytical Well Test Derivative for Line-X Seed Nodes for Carbonate Pore Network

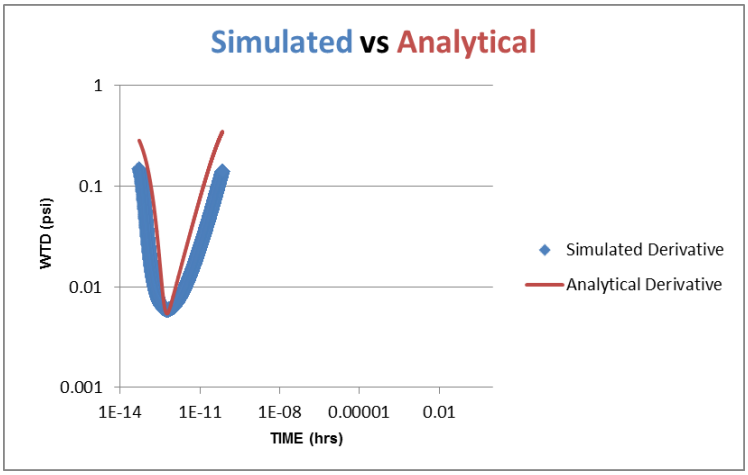

Figure 57: Match of the Simulated and Analytical Well Test Derivative for Line-Y Seed Nodes for Carbonate Pore Network

Table 13 shows an anisotropy occurs for the Line-Y seed node simulation. The least square residual of fit is quite small for Line-Y as compared to Line-X and Line-Z.

Direction	**Permeability (md)**	**Storativity ratio**	**Interporosity Flow Coefficient**	**Least Square Residual of fit**
Line-Z	1700	0.0008	0.0014	491
Line-X	1800	0.0002	0.0013	226
Line-Y	1300	0.0014	0.0004	97

Table 13: Permeability from Well Test Derivative Analysis for Different Directions for Carbonate Pore Network

4.2.2 Analysis using the Depth of Investigation Method

The Depth of Investigation (DOI) concept is used to get an estimate of the permeability in this method. A particular plane acts as seed nodes for the simulation to start. We have run the simulations for bottom-XY, left-YZ and front-XZ plane seed nodes for the carbonate pore network. The Figure 58 shows the different planar configurations of seed nodes used for DOI analysis.

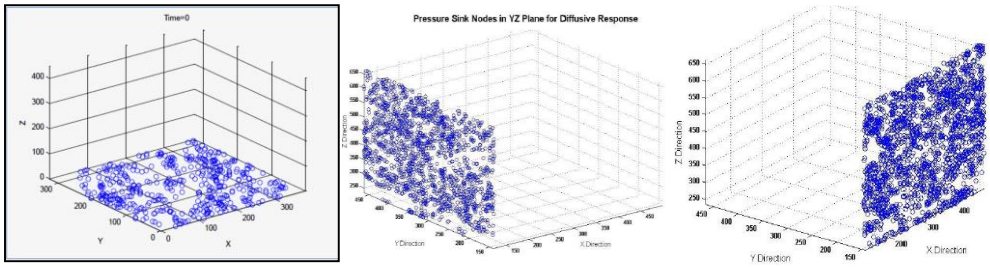

Figure 58: Bottom-XY, Left-YZ, Front-XZ Plane Seed Nodes (from Left to Right)

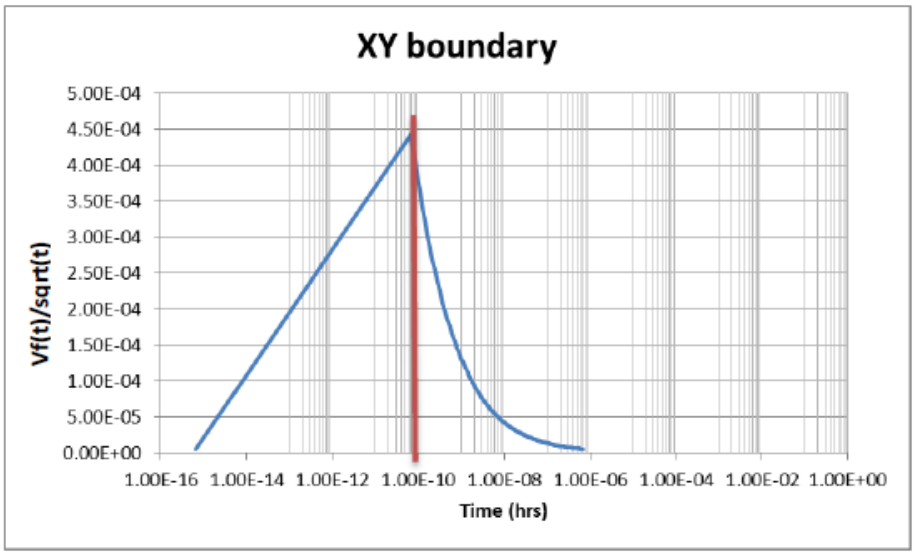

Figure 59: Vf(t)/$\sqrt{t}$ vs Time for Top XY Plane for Bottom XY Plane Seed Nodes for Carbonate Pore Network

Figure 59, Figure 60 and Figure 61 are the plots of Vf(t)/$\sqrt{t}$ for bottom-XY, left-YZ and front-XZ plane seed node configurations respectively. All these plots follow a similar pattern.

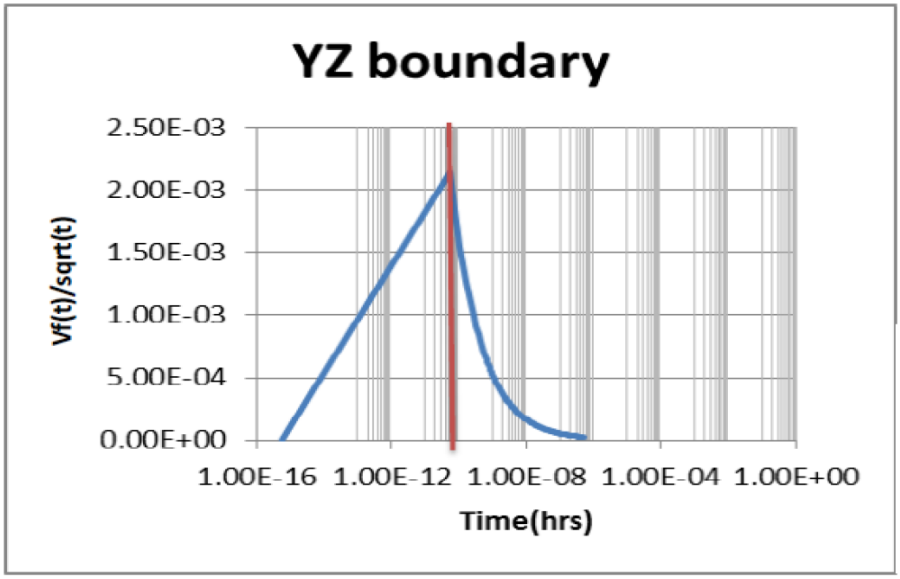

Figure 60: Vf(t)/$\sqrt{t}$ vs Time for Right YZ Plane for Left YZ Plane Seed Nodes for Carbonate Pore Network

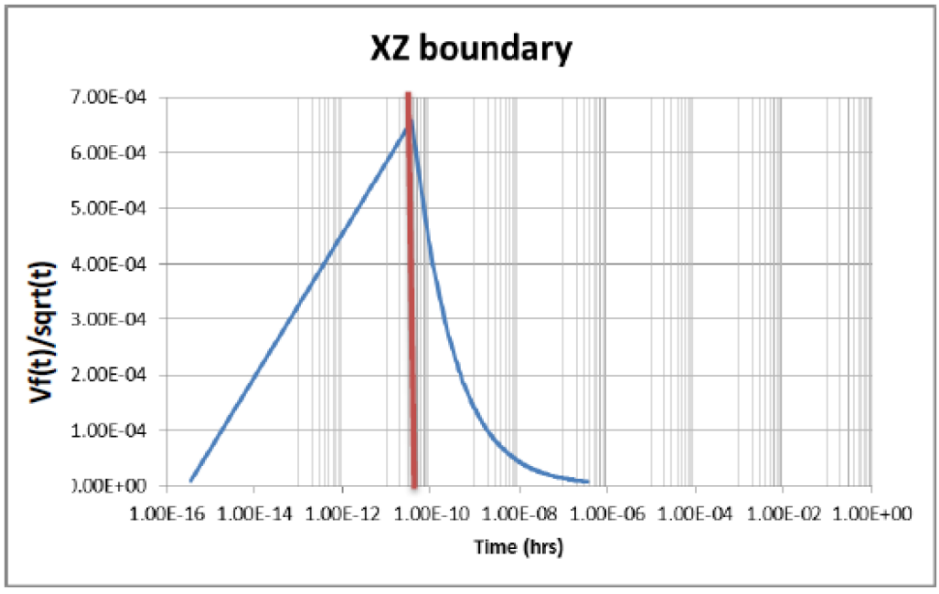

Figure 61: Vf(t)/$\sqrt{t}$ vs Time for Back XZ Plane for Front XZ Plane Seed Nodes for Carbonate Pore Network

Direction	DOI (m)	Time (hrs.)	Permeability (md)
YZ Plane	0.00754	5.43e-11	34300
XZ Plane	0.00644	3.59e-11	37200
XY Plane	0.00858	6.63e-11	36200

Table 14: Results from DOI Analysis in Carbonate Pore Network

The permeability values obtained from DOI analysis are quite high as compared to the values from steady state analysis and derivative analysis (Table 14). The DOI analysis is capturing the permeability value of the least DTOF path or the very well connected nodes in the networks which is reflected in the high permeability values. These paths are very less in number and will have very low cross sectional area due to the low storativity ratio values.

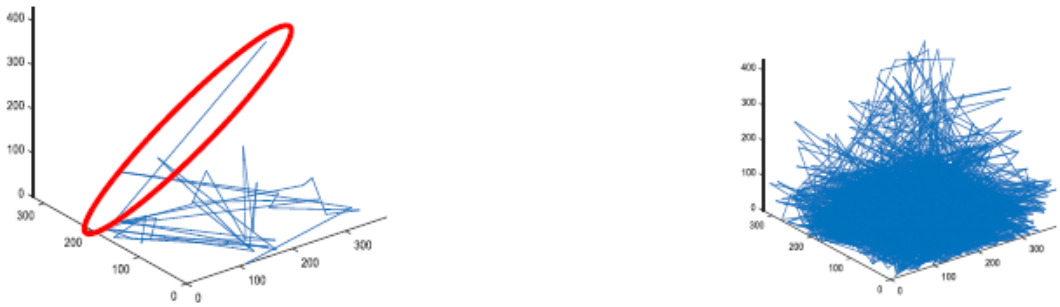

Figure 62: (a) The Least DTOF to the Top XY Plane for the Bottom XY Plane Seed Node Simulation, (b) The Maximum DTOF Path to the Top XY Plane Visualization for Bottom XY Plane Seed Node Simulation in Carbonate Pore Network

The Figure 62(a) shows the presence of a high permeability path in the pore network marked by the red ellipse. These kind of high permeability paths in the carbonate pore network gives high value of permeability in the DOI analysis.

A steady state analysis had also been done on this carbonate pore network as has been discussed in the literature review section. A comparison of the results from all these methods has been presented below (Table 15).

Well Test Derivative		**Steady State**		**DOI**	
Line X	1800 md	$\sqrt{\mathbf{Ky}.\mathbf{Kz}}$	1432 md	$\sqrt{\mathbf{Ky}.\mathbf{Kz}}$	36700 md
Line Y	1300 md	$\sqrt{\mathbf{Kx}.\mathbf{Kz}}$	1290 md	$\sqrt{\mathbf{Kx}.\mathbf{Kz}}$	35237 md
Line Z	1700 md	$\sqrt{\mathbf{Ky}.\mathbf{Kx}}$	1516 md	$\sqrt{\mathbf{Ky}.\mathbf{Kx}}$	35720 md

Table 15: Comparison of Results for the Carbonate Pore Network among the Well Test Derivative Analysis, Steady State and DOI Analysis Method

The steady state permeability values presented are the geometric averages of the planar permeability values because we are comparing them to line permeability values (Sec 3.2.2). The well test derivative permeability values are within 35% of the steady state permeability values. The DOI permeability values are quite high since these permeability values are representing the extremely small cross-sectional area high permeability paths that are present in the carbonate pore network.

5. SUMMARY AND CONCLUSION

We have developed a novel method to perform computational pressure transient analysis on pore network models which provide much more information than traditional steady state methods. This method has been validated on the synthetic sandstone model which was developed. The well test derivative analysis on the synthetic sandstone pore network gave results which were very close to the mean permeability of the bonds. The shape of the well test derivative curve accurately represented the flow regimes expected in a sandstone. The steady state permeability in the synthetic sandstone pore network was also very close to the mean permeability of the bonds. The permeability values obtained from the DOI analysis in the synthetic pore network was also close to the mean permeability of the bonds. The ratio of permeability values obtained from the transient techniques to the permeability value from the steady state technique was increasing with increasing heterogeneity.

The carbonate model was also analysed using these methods. The well test derivative curve showed distinct characteristics of dual porosity. This well test derivative curve was used to calculate the permeability using an analytical dual porosity model. The permeability values from the well test derivative analysis were quite close to those obtained from the steady state analysis. The DOI analysis method gave very high permeability values as compared with the other two methods because the wave front reaches the opposite plane following the path of the least DTOF or the highest permeability. Such high permeability paths are expected in a carbonate rock due to the presence of intergranular pore spaces. The permeability values obtained from DOI

analysis for the carbonate sample are more a reflection of these high permeability paths than the average permeability of the sample.

The DOI method captures the effect of the passage of a pressure wave through very high permeability paths in the pore network. These paths represent a very small area in the carbonate pore network as evidenced by the low storativity ratio values. The steady state technique captures the effect at long time values when the pressure wave has reached all parts of the pore network. The cross sectional area captured in the steady state technique is almost equal to the total cross-sectional area of the all the paths present in the pore network. Therefore, we will have to devise a transient technique based on average pressure drop across the complete pore network such that it captures the effect of the total cross-sectional area available to flow and not just the well-connected path areas.

The transient techniques provide an insight into the nature of the sample. The well test derivative analysis technique can easily distinguish between a dual porosity and a single porosity type of sample. The flow regime in reservoirs is rarely steady state unless water flooding is being done above bubble point. Moreover, the permeability determination techniques at the reservoir scale are based on transient methods. The extension of these methods to the pore scale level to determine permeability values is an important step towards the future. An area of application can be in the unconventional reservoirs. Tight gas or shale will practically never experience steady state flow regime. The transient methods can be used for the analysis of these unconventional reservoir core samples.

REFERENCES

1) Ahmad, S., Azad, A., & Loughlin, K. (2005, August). A study of permeability and tortuosity of concrete. In *30th conference on our world in concrete and structures*, 23-24.

2) American Association of Petroleum Geologists. (n.d.). Porosity. Retrieved January 31, 2016, from http://wiki.aapg.org/Porosity#Chttp://wiki.aapg.org/Porosity#Carbonate_pore_systemsarbonate_pore_systems

3) Argonne National Laboratories. (n.d.). TOTAL POROSITY. Retrieved January 20, 2016, from http://web.ead.anl.gov/resrad/datacoll/porosity.htm

4) Arns, J. Y., Sheppard, A. P., Arns, C. H., Knackstedt, M. A., Yelkhovsky, A., & Pinczewski, W. V. (2007). Pore-level validation of representative pore networks obtained from micro-ct images. In *Proceedings of the International Symposium of the Society of Core Analysts*.

5) Baumann, T., & Werth, C. J. (2004). Visualization and modeling of polystyrol colloid transport in a silicon micromodel. *Vadose Zone Journal*, *3*(2), 434-443.

6) Blunt, M. J., Jackson, M. D., Piri, M., & Valvatne, P. H. (2002). Detailed physics, predictive capabilities and macroscopic consequences for pore-network models of multiphase flow. *Advances in Water Resources*, *25*(8), 1069-1089.

7) Boek, E. S., & Venturoli, M. (2010). Lattice-Boltzmann studies of fluid flow in porous media with realistic rock geometries. *Computers & Mathematics with Applications*, *59*(7), 2305-2314.

8) Bourdet, D., Ayoub, J. A., & Pirard, Y. M. (1989). Use of pressure derivative in well test interpretation. *SPE Formation Evaluation*, *4*(02), 293-302.

9) Choquette, P. W., & Pray, L. C. (1970). Geologic nomenclature and classification of porosity in sedimentary carbonates. *AAPG bulletin*, *54*(2), 207-250.

10) Coles, M. E., Hazlett, R. D., Spanne, P., Soll, W. E., Muegge, E. L., & Jones, K. W. (1998). Pore level imaging of fluid transport using synchrotron X-ray microtomography. *Journal of Petroleum Science and Engineering*, *19*(1), 55-63.

11) Dijkstra, E. W. (1959). A note on two problems in connexion with graphs. *Numerische mathematik*, *1*(1), 269-271.

12) Dong, H. (2008). *Micro-CT imaging and pore network extraction* (Doctoral dissertation, Department of Earth Science and Engineering, Imperial College London).

13) Eliasson, S., & Lundberg, A. (2015). Effects of Martensitic Phase Transformation on Advancing Cracks in Austenitic Steel. *TFHF-5199*.

14) Fatt, I. (1956). The network model of porous media.

15) Hales, T. (2001). Cannonballs and Honeycomb (with overview and graphics by Gartside, P.). Retrieved January 20, 2016, from http://www.math.pitt.edu/articles/cannonOverview.html

16) Harris, P. M. (1985). Carbonate cementation—a brief review.

17) IHS Energy (Fekete Associates Inc.). (n.d.). Conventional Test Analyses. Retrieved January 20, 2016, from https://cdn.ihs.com/fekete/help/WellTest/content/html_files/analysis_types/conventional_test_analyses/conventional_test_analyses.htm

18) Kaviany, M. (2012). *Principles of heat transfer in porous media*. Springer Science & Business Media.

19) Kulkarni, K. N., Datta-Gupta, A., & Vasco, D. W. (2000, January). A streamline approach for integrating transient pressure data into high resolution reservoir models. In *SPE European Petroleum Conference*. Society of Petroleum Engineers.doi:10.2118/65120-MS

20) La Barck Jr, A. J. (2010). *A Computational Study of Blood Flow and Oxygen Transport During Reperfusion and Post-conditioning* (Doctoral dissertation, Rowan University).

21) Lee, J., & Wattenbarger, R. A. (1996). *Gas reservoir engineering*.

22) Lee, J., Rollins, J. B., & Spivey, J. P. (2003). *Pressure transient testing* (Vol. 9). Henry L. Doherty Memorial Fund of Aime Society of Petroleum.

23) Lee, W. J. (1982). Well Testing, Textbook Series. *Society of Petroleum Engineers*.

24) Lindquist, W. B., Lee, S. M., Coker, D. A., Jones, K. W., & Spanne, P. (1996). Medial axis analysis of void structure in three-dimensional tomographic images of porous media. *Journal of Geophysical Research: Solid Earth*, *101*(B4), 8297-8310.

25) Lindquist, W. B., Venkatarangan, A., Dunsmuir, J., & Wong, T. F. (1999). Pore and throat size distributions measured from synchrotron X-ray tomographic images of Fontainebleau sandstones.

26) Manwart, C., Aaltosalmi, U., Koponen, A., Hilfer, R., & Timonen, J. (2002). Lattice-Boltzmann and finite-difference simulations for the permeability for three-dimensional porous media. *Physical Review E*, *66*(1), 016702.

27) Neapolitan, R. E., & Naimipour, K. (2011). *Foundations of algorithms*. Jones & Bartlett Learning.

28) Nunna, K., Zhou, P., & King, M. J. (2015, February). Novel Diffuse Source Pressure Transient Upscaling. In *SPE Reservoir Simulation Symposium*. Society of Petroleum Engineers.

29) Okabe, H., & Blunt, M. J. (2004). Prediction of permeability for porous media reconstructed using multiple-point statistics. *Physical Review E*, *70*(6), 066135.

30) Pasumarti, A. L. (2014). *Exploring an Unstructured Lattice Representation for Carbonate Reservoir Characterization* (Master's Thesis, Texas A&M University).

31) Peaceman, D. W. (1983). Interpretation of well-block pressures in numerical reservoir simulation with nonsquare grid blocks and anisotropic permeability. *Society of Petroleum Engineers Journal*, *23*(03), 531-543.

32) Sethian, J. A. (1999). *Level set methods and fast marching methods: evolving interfaces in computational geometry, fluid mechanics, computer vision, and materials science* (Vol. 3). Cambridge university press.

33) Silin, D., & Patzek, T. (2006). Pore space morphology analysis using maximal inscribed spheres. *Physica A: Statistical mechanics and its applications*, *371*(2), 336-360.

34) Stewart, G., & Asharsobbi, F. (1988, January). Well test intepretation for naturally fractured reservoirs. In *SPE Annual Technical Conference and Exhibition*. Society of Petroleum Engineers.

35) Surdam, R. C., Dunn, T. L., MacGowan, D. B., & Heasler, H. P. (1989). Conceptual models for the prediction of porosity evolution, with an example from the Frontier Sandstone, Bighorn Basin, Wyoming. *Sandstone Reservoirs: Rocky Mountain Association of Geologists*, 7-21.

36) University of California Davis. (n.d.). Cubic Lattices and Close Packing. Retrieved January 20, 2016, from

http://chemwiki.ucdavis.edu/Textbook_Maps/General_Chemistry_Textbook_Maps/Map:_Chem1_(Lower)/07:_Solids_and_Liquids/7.8:_Cubic_Lattices_and_Close_Packinghttp://chemwiki.ucdavis.edu/Textbook_Maps/General_Chemistry_Textbook_Maps/Map%3A_Lower's_Chem1/07%3A_Solids_and_Liquids/7.8%3A_Cubic_Lattices_and_Close_Packing

37) University of Kiel. (n.d.). Tetrahedral Sites. Retrieved February 03, 2016, from http://www.tf.uni-kiel.de/matwis/amat/def_en/kap_1/illustr/t1_3_4.html

38) University of Rochester. (n.d.). EES203: Study Resources. Retrieved February 05, 2016, from http://www.sas.rochester.edu/ees/ees203/resources.html

39) Warren, J. E., & Root, P. J. (1963). The behavior of naturally fractured reservoirs. *Society of Petroleum Engineers Journal*, *3*(03), 245-255.

40) Wellington, S. L., & Vinegar, H. J. (1987). X-ray computerized tomography. *Journal of Petroleum Technology*, *39*(08), 885-898.

41) Weyl, P. K. (1960). Porosity through dolomitization: conservation-of-mass requirements. *Journal of Sedimentary Research*, *30*(1).

42) WolframAlpha. (n.d.). Cubic Close Packing. Retrieved January 31, 2016, from http://mathworld.wolfram.com/CubicClosePacking.html

43) Xie, J., Gupta, N., King, M. J., & Datta-Gupta, A. (2012, January). Depth of investigation and depletion behavior in unconventional reservoirs using fast marching methods. In *SPE Europec/EAGE Annual Conference*. Society of Petroleum Engineers.

44) Zhang, Y., Yang, C., King, M. J., & Datta-Gupta, A. (2013, February). Fast-marching methods for complex grids and anisotropic permeabilities: Application to unconventional reservoirs. In *SPE Reservoir Simulation Symposium*. Society of Petroleum Engineers.

45) Zhou, Y., & King, M. J. (2013, September). Impact of subsurface uncertainty on well placement in tight gas reservoirs: Application of a rapid simulation-free workflow. In *SPE Annual Technical Conference and Exhibition*. Society of Petroleum Engineers.

APPENDIX

APPENDIX A (Determination of Bond Lengths in the Synthetic Sandstone Pore Network)

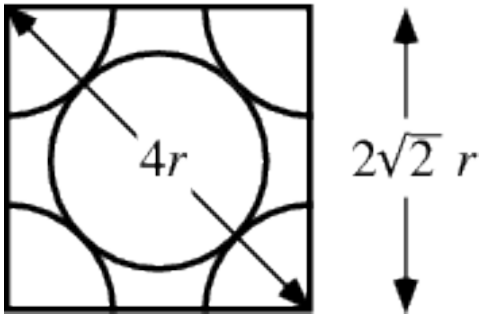

Figure 63: Dimension of a Face of the Synthetic Pore Network Unit Cell/ FCC Cell. R is the Grain Radius (R_{grain}) (Courtesy Wolfram Webpage on Cubic Close Packing)

There are two types of bonds in our synthetic sandstone pore network. One bond is from an edge octahedral node to a central octahedral node. Another type of bond is from a tetrahedral node to an octahedral node. We want to find the length of these bonds.

The octahedral node radius is given by, $r_{oct} = 0.414 * R_{grain}$

The tetrahedral node radius is given by, $r_{tet} = 0.225 * R_{grain}$

The unit cube edge length= $2\sqrt{2}R_{grain}$

Octahedral nodes on the edge are located at the center of each edge of the unit cubic cell (Figure 34).Length of the bond from the edge octahedral node to the central octahedral node= length from the edge center to the cube centroid- 2* radius of the octahedral node

$=\sqrt{2 * (\frac{2\sqrt{2}R_{grain}}{2} - 0)^2} - 2 * 0.414 * R_{grain}$=1.172*$R_{grain}$

Tetrahedral nodes are located ¼ th of the distance along the body diagonal away from each vertex of the unit cubic cell (Figure 34). We have to find the co-ordinates of tetrahedral node for which we need the length of the body diagonal and the angle between the body diagonal with the X, Y and Z planes.

The length of the body diagonal=$\sqrt{3 * (2\sqrt{2}R_{grain})^2}$=$2\sqrt{6}R_{grain}$

Angle of body diagonal with the X, Y and Z planes= 54.7^o

We can now compute the co-ordinates of tetrahedral void center located nearest to the vertex formed by the front XZ, left YZ and bottom XY planes are ($(\frac{1}{4} * 2\sqrt{6}R_{grain} * \cos(54.7^o), \frac{1}{4} * 2\sqrt{6}R_{grain} * \cos(54.7^o), \frac{1}{4} * 2\sqrt{6}R_{grain} * \cos(54.7^o))$

=$(\frac{R_{grain}}{\sqrt{2}}, \frac{R_{grain}}{\sqrt{2}}, \frac{R_{grain}}{\sqrt{2}})$.

The co-ordinates of centroid of cube are $(\sqrt{2}R_{grain}, \sqrt{2}R_{grain}, \sqrt{2}R_{grain})$.

Length of bond between tetrahedral node and central octahedral node = distance between center of tetrahedral node and centroid of unit cell cube – radius of tetrahedral node-radius of octahedral node

$=\sqrt{3 * (\frac{R_{grain}}{\sqrt{2}} - \sqrt{2}R_{grain})^2} - 0.414 * R_{grain} - 0.225 * R_{grain}$=0.5857*$R_{grain}$